universe

MDPI

Review

Mixing and Magnetic Fields in Asymptotic Giant Branch Stars in the Framework of FRUITY Models

Diego Vescovi

Institute for Applied Physics, Goethe University Frankfurt, Max-von-Laue-Strasse 1, 60438 Frankfurt am Main, Germany; vescovi@iap.uni-frankfurt.de

Abstract: In the last few years, the modeling of asymptotic giant branch (AGB) stars has been much investigated, both focusing on nucleosynthesis and stellar evolution aspects. Recent advances in the input physics required for stellar computations made it possible to construct more accurate evolutionary models, which are an essential tool to interpret the wealth of available observational and nucleosynthetic data. Motivated by such improvements, the FUNS stellar evolutionary code has been updated. Nonetheless, mixing processes occurring in AGB stars' interiors are currently not well-understood. This is especially true for the physical mechanism leading to the formation of the ^{13}C pocket, the major neutron source in low-mass AGB stars. In this regard, post-processing s-process models assuming that partial mixing of protons is induced by magneto-hydrodynamics processes were shown to reproduce many observations. Such mixing prescriptions have now been implemented in the FUNS code to compute stellar models with fully coupled nucleosynthesis. Here, we review the new generation of FRUITY models that include the effects of mixing triggered by magnetic fields by comparing theoretical findings with observational constraints available either from the isotopic analysis of trace-heavy elements in presolar grains or from carbon AGB stars and Galactic open clusters.

Keywords: nucleosynthesis; s-process; asymptotic giant branch stars; stellar abundances; nuclear reaction cross-sections; chemically peculiar stars; circumstellar dust; magnetic fields; galactic chemical evolution

Citation: Vescovi, D. Mixing and Magnetic Fields in Asymptotic Giant Branch Stars in the Framework of FRUITY Models. *Universe* **2022**, *8*, 16. https://doi.org/10.3390/universe8010016

Academic Editor: Jacco Th. van Loon

Received: 2 December 2021
Accepted: 22 December 2021
Published: 28 December 2021

1. Introduction

The synthesis of elements heavier than iron mostly takes place through neutron-capture processes. Depending on the reaction timescales of neutron captures, two main processes can be distinguished: the slow (s) process (see Käppeler et al. [1] for a review) and the rapid (r) process (see Cowan et al. [2] for a review). The s-process takes place under relatively low neutron density conditions ($N_n \sim 10^7$–10^{11} neutrons cm^{-3}) so that the time scale for neutron captures is much longer than the β-decay time scale of radioactive isotopes. As a consequence, nuclei produced through the *s*-process are located very close to the stability valley. On the contrary, the *r*-process proceeds on timescales shorter than β-decay timescales, thus synthesizing strongly β-unstable nuclei, up to the neutron-drip line. The Solar System abundances can be explained as a superposition of these two processes [3]. In particular, the abundance of about half of nuclei heavier than strontium is accounted for by slow neutron captures occurring in low- and, to a lesser degree, intermediate-mass stars ($M \lesssim 8\ M_\odot$).

In these stars, once the core He supply has been exhausted after the central He burning phase, and electron degeneracy has been set up in the resulting C-O core, He burning is established in a thin shell. The high energy production causes the overlying layers to expand and cool, and the above H-burning shell gradually becomes less active. In the H-R diagram, this early phase corresponds to the beginning of the asymptotic giant branch (AGB). The stellar structure then begins to shrink until the H-burning shell re-ignites. At the end of this stage, the star has a degenerate core of C-O that is growing in mass, two

burning shells of He and H that are separated from a He-rich intermediate zone in radiative equilibrium (He-intershell), and an expanded convective envelope. The helium produced by the H-burning shell accumulates, causing an increase of density and temperature in the innermost zones. As a result, over tens of thousands of years, the He-shell switches on in semi-explosive conditions. On the one hand, the energy released during this thermal pulse (TP) drives convective motions across the He-intershell region, homogenizing it with freshly synthesized He-burning products (helium, carbon, and heavy s-process elements). On the other hand, it causes an expansion, and thus, cooling of the H-shell, which eventually dies down, while He-burning continues in radiative conditions. Later on, the star contracts again, heating up and leading to the re-ignition of the H-shell. This alternating sequence of burning defines the thermally pulsing AGB (TP-AGB) phase of these stars. During envelope expansion, convection penetrates below the H-He discontinuity, beyond the region where the H-shell was active. As a result, convective motions carry the by-products of the fusion reactions to the surface, modifying the star's surface abundance distribution. This is referred to as the third dredge-up (TDU).

The He-burning shells of AGB stars is one of the astrophysical environments in which the s-process takes place (see, e.g., Busso et al. [4]). The other is represented by the He-burning cores and C-burning shells of massive stars (see Raiteri et al. [5] and references therein). During the interpulse period, the zone between the two burning shells is significantly enriched in ^{14}N produced by the H-burning shell in its outward advance. Such ^{14}N is then mixed downward into the helium shell during the ensuing convective thermal pulse and eventually converted into ^{22}Ne through a series of α-captures. If the temperature is high enough ($T \gtrsim 3 \times 10^8$ K), the ^{22}Ne(α, n)^{25}Mg reaction is triggered as well. Due to the high temperature required for this reaction to take place, neutron emission through this channel is only efficient in intermediate AGB stars ($M \gtrsim 4\ M_\odot$; see, for instance, Karakas and Lattanzio [6]). Those temperatures can be attained also during the latest TPs of less massive AGB stars, although the resulting neutron fluxes have only a little impact on the final distribution of s-element abundance [7]. The primary neutron source in AGB stars is actually provided by ^{13}C nuclei, which are burnt via the ^{13}C(α, n)^{16}O reaction. This involves the occurrence of both proton and α captures in the He-intershell. One of the challenges in modeling this neutron production channel is related to the production of ^{13}C itself. In fact, the amount of ^{13}C left in the ashes of the H-burning shell is not large enough to account for the observed neutron enrichment in evolved stars. Hence, during a TDU, some process responsible for the partial mixing of protons from the envelope into the ^{12}C-rich region must be at work. Protons would subsequently be captured by ^{12}C nuclei, resulting in the formation of a thin layer enriched in ^{13}C, the so-called ^{13}C pocket. Neutrons are then efficiently released, during the interpulse phase, at about $T \approx 9 \times 10^7$ K through the ^{13}C(α, n)^{16}O reaction [8], which therefore represents the main neutron source in low-mass AGB stars ($M \leq 3\ M_\odot$; see Busso et al. [4]).

The formation of the ^{13}C pocket is still a matter of in-depth research. While classical post-process models generally assume an ad hoc ^{13}C pocket [9,10], several physically-based approaches have recently been devised to model the partial mixing of proton-rich material from the convective envelope. They are briefly reviewed in Section 2. Besides the comprehension of the role played by hydrodynamic and magnetohydrodynamic phenomena usually neglected in standard stellar model computations, understanding the s-process nucleosynthesis in AGB stars requires the adoption of refined input physics data. In Section 3.1 the recent updates made to the FUNS code are outlined, along with a description of mixing triggered by magnetic fields, which is now included to account for the formation of the ^{13}C pocket in FRUITY models. New magnetic FRUITY models of low-mass stars computed with the FUNS code are presented in Section 4. A thorough comparison with available high-accuracy data from laboratory measurements of presolar meteoritic grains, observational data for intrinsic and extrinsic AGB stars, and heavy elements abundance in Galactic open clusters is also described. Conclusions are drawn in Section 5.

2. Mixing Processes in AGB Stars

The circulation of material in stars is tightly linked to the transport of energy. The main modes of energy transport are radiation and, in degenerate conditions, electron conduction. To these, we must add a third form of energy flow contribution, namely convection. Convection is a process for transporting energy and chemical elements in star interiors that involves large-scale motions of matter. If we imagine that bubbles of matter move within the star, then turbulence will mediate the creation and destruction of these bubbles. Since a full description of the convective mixing processes is computationally too expensive, usually one relies on the phenomenological mixing length theory (MLT) [11]. In standard stellar models, convection is the sole process considered for transporting chemical elements. However, such models with pure convection have been demonstrated to be incapable of reproducing AGB isotopic and elemental distributions, which therefore can provide constraints on the velocity and, possibly, the nature of the mixing phenomena that are taking place. This is particularly the case of processes driving to the synthesis of neutron-rich elements that occurs during the TP-AGB phase (see., e.g., Cristallo et al. [7,12], Trippella et al. [13]). In this regard, one of the open questions concerns the formation of the ^{13}C pocket, the answer to which is closely related to understanding the physical mechanisms driving mass exchange at the boundary between the convective envelope and the radiative core. Recent studies have concentrated on non-convective additional transport processes, ranging from diffusive to quite rapid dynamic and magnetohydrodynamic mixing, which are often ignored by the canonical theory of stellar structure and evolution.

One kind of additional transport process is represented by convective overshooting [14]. When the convective envelope approaches the H-exhausted zone during a TDU, the innermost layers become unstable owing to the creation of a sharp chemical discontinuity (see, e.g., Frost and Lattanzio [15]). Because of the chemical gradient, the turbulent eddies of the convective envelope have a high average radial velocity and may overshoot beyond the Schwarzschild limit, reaching the underlying stable layers and inducing some extra-mixing. Convective overshooting is usually described in stellar evolution calculations as an exponential decrease of the diffusion coefficient [14,16] or the convective velocities [12,17], depending on the numerical algorithm used for chemical transport (see also Goriely and Siess [18]). The aforementioned exponential profile has firstly been found in hydrodynamic simulations by Freytag et al. [19]. Based on two-dimensional hydrodynamic simulations [20], the Ref. Battino et al. [21,22] used a double exponential decreasing profile to account for Kelvin-Helmholtz instabilities as well as internal gravity waves (IGWs) mixing [23] at the bottom of the convective envelope. The resulting predictions for heavy s-process enhancements agree with the majority of the observational data but have issues in reproducing the entire ranges of some isotope ratios recorded in presolar grains unless some additional rotation-induced mixing is invoked [22].

Rotation is actually recognized to have an effect on the dynamic processes at work in stellar interiors (e.g., Maeder [24]). Many constraints on these processes have been established by helioseismology and asteroseismology (see Aerts [25] for a review). Furthermore, rotation, and particularly differential rotation, induces various instabilities that result in mixing processes capable of transporting materials from the inner layers to the surface. Although it is evident that stars rotate and that rotation can cause several instabilities that might lead to mixing, it is uncertain how efficient these processes are and how the various instabilities interact with each other (see, for example, Maeder [24]). Rotation-induced mixing in AGB stars has been examined extensively [26–29]. These studies raised doubts on the capacity of rotation alone to induce a sizable ^{13}C pocket. Nonetheless, a variation in the initial rotational velocity might lead to a change in the final surface s-process enhancements and spectroscopic indexes, if the star rotates fast enough [29]. On the other hand, AGB models rotating at a rate that matches the asteroseismic measurements, show an s-process production comparable to that of the non-rotating model [29,30], questioning that mixing induced by rotation may still play a significant role in s-process nucleosynthesis in low-

mass AGB stars. That said, other processes triggered by rotation may play an important role in mixing processes inside AGB stars.

As a matter of fact, a phenomenon strictly connected to rotation is stellar magnetism. The latter is often neglected in the computation of stellar evolutionary models. However, the interplay between convection and stellar differential rotation can generate complex internal magnetic fields that may play a major role in the evolution of stars. Such internal magnetic fields can be grouped into two different categories. The first deals with fossil fields, which are relics of the star formation process that have managed to survive in a stable configuration. The other type is related to time-dependent magnetic fields generated and sustained by a dynamo process, taking advantage of energy sources such as convection and/or differential rotation. The latter could produce a self-sustained small-scale magnetic field in a radiative zone (see, e.g., Braithwaite and Spruit [31]) which could also be responsible for the transport of angular momentum and chemical elements [32,33]. This is e.g., the case of mixing induced by magnetic buoyancy [32,34]. This theory advances the hypothesis that the dynamo-generated buoyancy of magnetized material might offer a physical mechanism for transporting material from the radiative regions to the above convective envelope of low-mass stars during the RGB and AGB phases. In this scenario, the original poloidal field of a rotating star generates a strong toroidal field developing various instabilities [35,36] among which the buoyancy of magnetized structures (e.g., Schuessler [37]). Such magnetic instabilities may also supply a sufficient mass transport rate capable to explain the formation of the ^{13}C pocket in TP-AGB stars [13,38,39]. Therefore, the presence of magnetic fields adds new transport mechanisms, some of which could compete with or suppress purely hydrodynamic processes and could alter stellar surface element distributions (see Section 4).

3. Updating FRUITY Stellar Models

3.1. Input Physics

Solving the system of equations that defines the stellar structure requires the knowledge of the equation of state (EOS), opacity, and mass/energy losses/gains as a function of temperature, density, and chemical composition for the typical conditions of stellar interiors. In the past few years, the great advance in computing power allowed to provide larger and larger stellar yield sets from detailed AGB models (see, e.g., Ventura et al. [40], Herwig [41], Karakas and Lattanzio [42], Cristallo et al. [43], Ritter et al. [44]). In this regard, stellar evolutionary tracks of low- and intermediate-mass stars from the pre-main sequence to the AGB tip are usually computed using a reduced nuclear network, while the nucleosynthesis calculations of heavy s-process elements are confined to post-processing techniques. An exception is represented by the FUNS code [17], in which the physical evolution of the star is coupled to a full nuclear network including all relevant isotopes up to the termination point of the s-process path. The chemical and physical features of the stellar models obtained with the FUNS code are collected in the FRUITY (FUNS Repository of Updated Isotopic Tables & Yields) online database [7,43], which is, at present, one of the most complete available databases for the s-process in AGB stars in terms of the range of masses and metallicities. During recent years, the FUNS code has been extensively updated with the state of the art of input physics available in the literature. In the following, we briefly report the major updates to the EOS, the heavy-element admixture, the opacity tables, the mass-loss rate, and the nuclear reaction network.

Regarding the EOS, in its latest version, FUNS employs two different EOS valid in different physical conditions, provided as pre-computed tables to be interpolated. For $\log T$ [K] < 6.5 the most recent version of the OPAL EOS [45] (updated in 2005) is adopted. To correctly describe high-density plasma in which electrons must be treated as degenerate particles and configurations where hydrogen is absent are reached, such as He, C, and O cores during RGB and AGB phases, the EOS for fully ionized given by Straniero [46], in the form updated by Prada Moroni and Straniero [47], is used for $\log T$ [K] $\geq$ 6.5.

For the heavy element mixture, that is, the abundance distribution of the chemical elements heavier than helium, FUNS utilizes the proto-solar abundance distribution given

by Lodders [48] for close-to-solar metallicity stars, while for metal-deficient objects, a given amount of α-enhancement is adopted (see Vescovi et al. [49] for more details).

Similar to the EOS, the opacity coefficients are given as pre-computed tables, covering a wide range of densities and temperatures. The opacity is strongly dependent on the relative abundances of the various elements and the specific solar mixture adopted. In the more advanced RGB and AGB phases, when the stellar structure develops a core with partial degenerate electrons (helium or carbon core), electron conduction becomes the predominant mechanism for energy transport and must be considered to total opacity. Conversely, in the cool external layers of stars, the formation of molecules ($T \lesssim$ 4500–4000 K) presenting many absorption lines, increases the radiative opacity. In the present version of the FUNS code, we adopt the most recent version of the OPAL radiative opacity tables [50] for $\log T[\mathrm{K}] > 4.05$. The final opacity tables have then been obtained by adding the conductive opacity computed by Potekhin et al. [51], Shternin and Yakovlev [52]. For lower temperatures ($\log T\ [\mathrm{K}] \leq 4.05$), typical of the external layers of stars, we used the ÆSOPUS tool [53] to compute the opacity tables in order to take into account the chemical composition variations of the envelope occurring during the TP-AGB phase. The present opacity tables have been calculated for the updated solar admixture of Lodders [48] and for (eventual) considered α-enhancement.

In the late stage of low- and intermediate-mass stars evolution, mass loss induces important changes in the stellar properties. During the AGB phase, large-amplitude pulsations cause the compression of the outer atmospheric layers and the formation of molecules and dusty particles leading the star to lose mass conspicuously due to strong stellar winds [54]. Such mass loss directly affects the duration of the AGB phase, the strength of the pulse, and the efficiency of the TDU [6,17,55]. For the practical purposes of stellar evolution computations, the effect of mass loss is usually included by means of empirical or semi-empirical formulas. In particular, the AGB mass-loss rate can be estimated from the observational correlation with the pulsation (see, e.g., Vassiliadis and Wood [56]). In past FRUITY models [7,12,17,43], the mass-loss law was obtained by fitting the mass-loss rate versus period for a sample of Galactic O-rich and C-rich giants. The stellar period is computed employing the relation between the magnitude in the K band and period provided by Whitelock et al. [57]. The bolometric magnitude of the model is then calculated by applying a bolometric correction (BC_K) as a function of the effective temperature (T_{eff}). In new FRUITY models, we adopt a new fit given by Abia et al. [58], who considered an updated T_{eff} dataset of O-rich red giants from Buzzoni et al. [59] and a new BC_K vs. T_{eff} relation.

The calculation of nuclear processes in stellar plasma is a fundamental aspect for the integration of a stellar model: in addition to defining the energy generated and thus establishing the balance of a stellar structure, nuclear reactions are also responsible for the chemical evolution of the star. The standard version of the FUNS code nuclear network follows the chemical evolution of almost 500 isotopes (from hydrogen to bismuth) linked by more than 800 reactions (charged particle reactions, neutron captures, and β-decays). The baseline nuclear network is essentially the same already described in the Ref. Cristallo et al. [12] with the inclusion of some recent updated reaction rates. All the updated charged particle reactions and neutron capture reactions are shown in Tables 1 and 2, respectively.

In addition, (n, γ) reaction rates for ^{61}Ni, ^{74}Se, ^{79}Kr, ^{81}Kr, ^{83}Kr, ^{84}Sr, ^{93}Nb, ^{94}Nb, ^{103}Rh, ^{109}Ag, ^{119}Sn, ^{121}Sn, ^{122}Sb, ^{125}Te, ^{129}I, ^{129}Xe, ^{142}Pr, ^{147}Pm, ^{151}Eu, ^{152}Eu, ^{153}Eu, ^{154}Eu, ^{158}Gd, ^{158}Dy, ^{169}Tm, ^{171}Tm, ^{170}Yb, ^{181}Hf, ^{181}Ta, ^{182}Ta, ^{182}W, ^{183}W, ^{189}Os, ^{192I}r, ^{193}Ir, ^{193}Pt, ^{205}Pb, and ^{210}Bi have been recomputed by using the updated stellar enhancement factor (SEF) from the KADoNiS v0.3 database [60]. The new β-decay rate for ^{60}Fe is from Rugel et al. [61]. The ^{60}Fe(n, γ) cross-section is from Uberseder et al. [62] and renormalized to take into account the new half-life of ^{60}Fe from Rugel et al. [61]. For the ^{7}Be electron-capture rate, we use that computed by Simonucci et al. [63] and provided in the tabulated form by Vescovi et al. [64]. The effects induced by the adoption of further re-evaluated neutron-capture cross-sections,

as provided by Reifarth et al. [65], on the s-process nucleosynthesis in low-mass AGB stars has been recently investigated in the context of FRUITY models [66].

Table 1. Updated charged particle reactions included in the FUNS's nuclear network.

Reaction	Reference	Reaction	Reference	Reaction	Reference
^{7}Li(p, α)^{4}He	[67]	^{23}Na(p, γ)^{24}Mg	[68]	^{16}O(α, γ)^{20}Ne	[69]
^{15}N(p, γ)^{16}O	[70]	^{23}Na(p, α)^{20}Ne	[71]	^{18}O(α, γ)^{22}Ne	[71]
^{17}O(p, γ)^{18}F	[72]	^{24}Mg(p, γ)^{25}Al	[71]	^{22}Ne(α, n)^{25}Mg	[73]
^{17}O(p, α)^{14}N	[74]	^{25}Mg(p, γ)^{26}Al^{g}	[75]	^{22}Ne(α, γ)^{26}Mg	[73]
^{14}C(p, γ)^{15}N	[71]	^{25}Mg(p, γ)^{26}Al^{m}	[75]	^{14}N(α, p)^{17}O	[76]
^{18}O(p, γ)^{19}F	[77]	^{26}Mg(p, γ)^{27}Al	[71]	^{15}N(α, γ)^{19}F	[71]
^{18}O(p, α)^{15}N	[78]	^{26}Al^{g}(p, γ)^{27}Si	[71]	^{17}O(α, γ)^{21}Ne	[79]
^{19}F(p, α)^{16}O	[80]	^{27}Al(p, γ)^{28}Si	[71]	^{17}O(α, n)^{20}Ne	[79]
^{9}Be(p, α)^{6}Li	[81]	^{27}Al(p, α)^{24}Mg	[71]	^{18}O(α, n)^{21}Ne	[82]
^{10}B(p, α)^{7}Be	[81]	^{4}He(2α, γ)^{12}C	[83]	^{19}F(α, p)^{22}Ne	[84]
^{20}Ne(p, γ)^{21}Na	[71]	^{12}C(α, γ)^{16}O	[85]	^{20}Ne(α, γ)^{24}Mg	[71]
^{21}Ne(p, γ)^{22}Na	[71]	^{13}C(α, n)^{16}O	[86]	^{24}Mg(α, γ)^{28}Si	[71]
^{22}Ne(p, γ)^{23}Na	[87]	^{14}C(α, γ)^{18}O	[88]		
^{22}Na(p, γ)^{23}Mg	[89]	^{14}N(α, γ)^{18}F	[71]		

Table 2. Updated neutron-capture reactions included in the FUNS's nuclear network.

Reaction	Reference	Reaction	Reference	Reaction	Reference
^{13}C(n, γ)^{14}C	[90]	^{75}As(n, γ)^{76}As	[91]	^{176}Lu(n, γ)^{177}Lu	[92]
^{14}N(n, p)^{14}C	[90]	^{79}Br(n, γ)^{80}Br	[93]	^{174}Hf(n, γ)^{175}Hf	[94]
^{17}O(n, α)^{14}C	[95]	^{81}Br(n, γ)^{82}Br	[93]	^{176}Hf(n, γ)^{177}Hf	[96]
^{19}F(n, γ)^{20}F	[97]	^{78}Kr(n, γ)^{79}Kr	[98]	^{177}Hf(n, γ)^{178}Hf	[96]
^{20}Ne(n, γ)^{21}Ne	[99]	^{80}Kr(n, γ)^{81}Kr	[98]	^{178}Hf(n, γ)^{179}Hf	[96]
^{21}Ne(n, γ)^{22}Ne	[99]	^{84}Kr(n, γ)^{85}Kr	[98]	^{179}Hf(n, γ)^{180}Hf	[96]
^{22}Ne(n, γ)^{23}Ne	[99]	^{84}Km(n, γ)^{85}Kr	[98]	^{180}Hf(n, γ)^{181}Hf	[96]
^{23}Na(n, γ)^{24}Na	[100]	^{86}Kr(n, γ)^{87}Kr	[98]	^{182}Hf(n, γ)^{183}Hf	[94]
^{24}Mg(n, γ)^{25}Mg	[101]	^{85}Rb(n, γ)^{86}Rb	[93]	^{180}W(n, γ)^{181}W	[102]
^{25}Mg(n, γ)^{26}Mg	[103]	^{87}Rb(n, γ)^{88}Rb	[93]	^{184}W(n, γ)^{185}W	[104]
^{26}Mg(n, γ)^{27}Mg	[101]	^{88}Sr(n, γ)^{89}Sr	[105]	^{186}W(n, γ)^{187}W	[104]
^{35}Cl(n, γ)^{36}Cl	[106]	^{90}Zr(n, γ)^{91}Zr	[107]	^{184}Os(n, γ)^{185}Os	[102]
^{40}Ar(n, γ)^{41}Ar	[108]	^{91}Zr(n, γ)^{92}Zr	[109]	^{186}Os(n, γ)^{187}Os	[110]
^{41}K(n, γ)^{42}K	[111]	^{92}Zr(n, γ)^{93}Zr	[112]	^{187}Os(n, γ)^{188}Os	[110]
^{40}Ca(n, γ)^{41}Ca	[113]	^{93}Zr(n, γ)^{94}Zr	[114]	^{188}Os(n, γ)^{189}Os	[110]
^{45}Sc(n, γ)^{46}Sc	[111]	^{94}Zr(n, γ)^{95}Zr	[115]	^{190}Os(n, γ)^{191}Os	[116]
^{54}Fe(n, γ)^{55}Fe	[117]	^{96}Zr(n, γ)^{97}Zr	[118]	^{192}Os(n, γ)^{193}Os	[116]
^{58}Fe(n, γ)^{59}Fe	[119]	^{96}Ru(n, γ)^{97}Ru	[120]	^{190}Pt(n, γ)^{191}Pt	[102]
^{59}Co(n, γ)^{60}Co	[119]	^{102}Ru(n, γ)^{103}Ru	[120]	^{192}Pt(n, γ)^{193}Pt	[121]
^{58}Ni(n, γ)^{59}Ni	[122]	^{104}Ru(n, γ)^{105}Ru	[120]	^{194}Pt(n, γ)^{195}Pt	[121]
^{60}Ni(n, γ)^{61}Ni	[123]	^{102}Pd(n, γ)^{103}Pd	[124]	^{195}Pt(n, γ)^{196}Pt	[121]
^{62}Ni(n, γ)^{63}Ni	[125]	^{120}Te(n, γ)^{121}Te	[124]	^{196}Pt(n, γ)^{197}Pt	[121]
^{63}Ni(n, γ)^{64}Ni	[126]	^{130}Ba(n, γ)^{131}Ba	[124]	^{198}Pt(n, γ)^{199}Pt	[116]
^{64}Ni(n, γ)^{65}Ni	[119]	^{132}Ba(n, γ)^{133}Ba	[124]	^{197}Au(n, γ)^{198}Au	[127]
^{63}Cu(n, γ)^{64}Cu	[128]	^{139}La(n, γ)^{140}La	[129]	^{196}Hg(n, γ)^{197}Hg	[102]
^{65}Cu(n, γ)^{66}Cu	[130]	^{151}Sm(n, γ)^{152}Sm	[131]	^{202}Hg(n, γ)^{203}Hg	[116]
^{64}Zn(n, γ)^{65}Zn	[132]	^{154}Gd(n, γ)^{155}Gd	[133]	^{204}Hg(n, γ)^{205}Hg	[116]
^{70}Zn(n, γ)^{71}Zn	[132]	^{156}Dy(n, γ)^{157}Dy	[124]	^{204}Pb(n, γ)^{205}Pb	[134]
^{73}Ge(n, γ)^{74}Ge	[135]	^{168}Yb(n, γ)^{169}Yb	[102]	^{206}Pb(n, γ)^{207}Pb	[136]
^{74}Ge(n, γ)^{75}Ge	[91]	^{174}Yb(n, γ)^{175}Yb	[116]	^{207}Pb(n, γ)^{208}Pb	[137]
^{76}Ge(n, γ)^{77}Ge	[91]	^{176}Yb(n, γ)^{177}Yb	[116]	^{209}Bi(n, γ)^{210}Bi	[138]

By using the aforementioned choices for the opacity tables, EOS, and nuclear reaction rates, we computed a standard solar model (for more details on the followed procedure see

Vescovi et al. [64,139]) to extract the initial solar helium and metallicity abundances, that are $Y = 0.267$ and $Z = 0.0167$, respectively. The corresponding mixing length parameter was found to be $\alpha_{\rm MLT} = 1.86$. Such values are adopted for computing solar metallicity FRUITY models. Different values for Y and Z adopted in calculating models at different metallicities are reported in Vescovi et al. [49].

3.2. Magnetic-Buoyancy-Induced Mixing and the ^{13}C Pocket Formation

The appearance of carbon and s-process heavy elements on the surface of AGB stars is related to the interplay of mixing and nuclear processes occurring in their interiors, but the physical mechanism that drives the creation of a ^{13}C pocket remains uncertain (see Section 1). In past FRUITY models, the opacity-induced overshoot [12,17] was adopted for modeling the partial mixing of hydrogen from the envelope required to synthesize fresh ^{13}C. According to the MLT, the average convective velocity is proportional to the difference between the radiative ($\bigtriangledown_{\rm rad}$) and the adiabatic ($\bigtriangledown_{\rm ad}$) temperature gradients. At the convective boundary, this quantity, and hence the average velocity, suddenly decreases to zero. However, some convective plumes may reach the underlying radiative and stable layer, resulting in some extra-mixing. During a TDU episode, the steep chemical gradient between the opaque H-rich convective envelope and the H-exhausted region below causes $\bigtriangledown_{\rm rad}$ to exceed $\bigtriangledown_{\rm ad}$ at the convective envelope's inner border which, therefore, becomes unstable. Then, driven by their inertia, the convective plumes overshoot beyond the formal Schwarzschild boundary, causing extra-mixing and the creation of a chemically smooth transition zone between the convective envelope and the radiative region. In FUNS, the mixing exerted by convective overshooting is computed by solving a time-dependent mixing equation [17,140], in which the average convective velocity is determined according to the MLT [11]. The Schwarzschild criterion is used to identify the convective boundary. The velocity of the descending material pushed by convection is evaluated at the inner border of the convective envelope as

$$v = v_{\rm cb} \exp\left(-\frac{\delta r}{\beta H_P}\right), \quad (1)$$

where δr is the distance from the convective border, while $v_{\rm cb}$ and H_P are the velocity and the pressure scale height at the convective border, respectively. β is a free parameter adjusted to 0.1 to maximize s-process production in low-mass AGB stars (see Cristallo et al. [12], Guandalini and Cristallo [141] for more details). The β parameter controls the amount of protons mixed beyond the convective boundary, as well as the TDU efficiency. In standard FRUITY models, the partially mixed zone extends over 2 $H_{\rm P}$ beyond the Schwarzschild limit [17], while in FRUITY Tail models [142], it extends up to the layer where the convective velocity is 10^{-11} times lower than the value reached at the Schwarzschild border. The resulting ^{13}C pocket was found to be much larger than the one generated in standard FRUITY models, leading to a significant increase in surface s-process enrichment, but without altering the TDU efficiency. FRUITY models computed by adopting $\beta = 0.1$ were shown to be able to reproduce the bulk of the luminosity function of Galactic C-stars [141] and the solar distribution of s-only isotopes [143]. More recently, the inclusion of the updates described in Section 3.1 led Vescovi et al. [144] to conclude that setting the β parameter to 0.1 would lead to an excessive TDU efficiency and found that it has to be reduced down to 0.025 to reproduce standard FRUITY results. On the other hand, this parameter option leads to a so weak partial mixing of hydrogen that almost no ^{13}C and so s-process nuclei are synthesized. Thus, mixing driven by magnetic fields has been included in the FUNS code as the source of extra-mixing required for the formation of the ^{13}C pocket.

The magnetic-buoyancy-induced mixing is implemented in the FUNS hydrostatic stellar evolutionary code, starting from the magnetic buoyancy model of Nucci and Busso [34]. Following these authors, it assumed that a toroidal field is present in the radiative He-intershell at the beginning of the TDU and triggers the buoyant rise of magnetic flux tubes

(see also Trippella et al. [13]). The toroidal field is supposed to be generated by a dynamo working in the AGB interiors, which amplifies a tiny seed poloidal field by draining the available differential rotation energy [32,145,146]. The Ref. Nucci and Busso [34] showed that the complex MHD equations valid for a stellar plasma may be considerably simplified for the particular geometry of the radiative layers underneath an evolved star's convective envelope. In this scenario, since the density distribution of the plasma can be approximated with a power law as a function of the radius ($\rho(r) \propto r^k$) with an exponent k that is negative and has a modulus larger than unity, the system of equations can be analytically solved, providing simple formulas that can be used in stellar models to simulate the local effects generated by the magnetic field. Under these conditions, the radial velocity of magnetized structures turns out to be

$$v(r) = v_{\rm p}\left(\frac{r_{\rm p}}{r}\right)^{k+1}, \tag{2}$$

where $r_{\rm p}$ refer to the radial position of the innermost layer where a magnetic flux tube, formed in the He-intershell region due to the buoyancy instability, starts to rise, while v_p is its initial buoyant velocity. k is the exponent in the relation $\rho \propto r^k$ and it is typically lower than -3 in the He-rich radiative layers below the convective envelope of an AGB star, when the H-burning shell is extinguished during a TDU episode (see also Busso et al. [147]). The above process outlines a mass up-flow, forced by magnetic buoyancy, that causes a down-flow of protons from the envelope for mass conservation. The ensuing down-flow velocity is

$$v(r) = u_{\rm p}\left(\frac{r_{\rm p}}{r}\right)^{k+2}, \tag{3}$$

where $u_{\rm p} \equiv f \cdot v_{\rm p}$ is the effective starting buoyant velocity (see Vescovi et al. [144] for more details). The filling factor f, that is, the fraction of the total mass of the stellar layer occupied by the magnetized domains, is of the order of 10^{-5} [13,32].

The critical toroidal B_φ required for the emergence of magnetic buoyancy instabilities can be used to identify $r_{\rm p}$ [144] and it can be expressed as [36,146,148]

$$B_\varphi = \left(4\pi\rho r N^2 H_{\rm p}\frac{\eta}{K}\right)^{1/2}, \tag{4}$$

provided that the field gradient is smooth, that is, $\partial \ln B_\varphi / \partial \ln r \sim O(1)$. Here N is the adiabatic Brunt-Väisälä frequency, η the magnetic diffusivity, K the thermal diffusivity and $H_{\rm p}$ the local pressure scale height. The critical B_φ, at the moment of the maximum penetration of the H-rich envelope during a TDU, varies from $\sim 10^4$ G to a few 10^5 G, in the region of interest for the formation of a ^{13}C pocket [144]. The position at which the pre-existing magnetic field exceeds B_φ determines the radial position of the layer from which buoyancy (on average) starts, thus defining the extension of the mixed zone and of the ^{13}C pocket. Therefore, the efficiency of magnetic-buoyancy-induced mixing depends on both the critical toroidal B_φ and the effective buoyant velocity $u_{\rm p}$, whose values have to be calibrated (see Section 4.1).

The updated input physics data, network, and mixing velocity described in this Section were used to calculate the evolutionary sequence of 1.5 and 2 $M_\odot$ stars at different metallicities presented in Vescovi et al. [49], Vescovi et al. [144], Magrini et al. [149] and that are recapped in Section 4.

4. Nucleosynthesis and Chemical Enrichment in Magnetic FRUITY Models

4.1. SiC Grains

AGB stars are major polluters of the ISM. The cool layers above their surface host the formation of solid dust grains, whose composition is determined by the relative elemental and isotopic abundances in the stellar atmosphere. About 90% of presolar silicon carbide (SiC) grains, representing the so-called mainstream (MS) group, are thought to come from ancient C-rich AGB stars that evolved prior to the formation of the Solar System (see Zinner [150] for a review). Thus, they keep a record of nucleosynthesis and mixing events

in their parent stars, providing clues on the stellar processes at play, provided that we are able to identify the kind of stars they originated from. In particular, isotopic s-element abundance ratios measured in these grains have been shown to offer accurate constraints on the ^{13}C pocket (e.g., Liu et al. [151]). According to the Si isotope ratios of MS grains, their parent stars should have close-to-solar (e.g., Hoppe et al. [152]) or slightly super-solar metallicity [153]. In particular, chemical and chemo-dynamical models of the Galaxy, properly combined with dust yields resulting from AGB models, showed that the bulk of presolar SiC grains originated from AGB stars with $M \sim 2\ M_{\odot}$ and $Z \sim Z_{\odot}$ [154,155]. On the other hand, the extremely rare μm-sized MS SiC grains may originate from AGB stars with nearly twice the solar metallicity of the Sun [156].

FRUITY Magnetic models for 2 $M_{\odot}$ AGB stars with close-to-solar metallicities with a single configuration for the toroidal field strength ($B_{\varphi} = 5 \times 10^4$ G) and the initial buoyant velocity ($u_{\rm p} = 5 \times 10^{-5}$ cm s^{-1}) consistently reproduce the majority of the heavy-element isotope ratios measured in presolar SiC grains from AGB stars. In Figure 1, we compare FRUITY Magnetic models with available laboratory measurements of isotope ratios for Ni, Sr, Zr, Mo, and Ba in presolar SiC grains. The isotope ratios are given using the standard δ-notation, which is defined as the variation, in parts per thousand, of the isotopic ratio measured in a grain relative to the terrestrial ratio. The Mo isotope data are instead reported in the usual spectroscopic notation. The capability of FRUITY Magnetic models of matching grain data can be understood by focusing on the trends of ^{88}Sr and ^{138}Ba isotopes. Previous studies using post-processing s-process models found that ^{13}C pockets with a flat ^{13}C profile and masses larger than a few 10^{-4} $M_{\odot}$ are needed to explain the bulk of mainstream SiC grains with negative ^{88}Sr/^{86}Sr and ^{138}Ba/^{136}Ba isotope ratios [151].

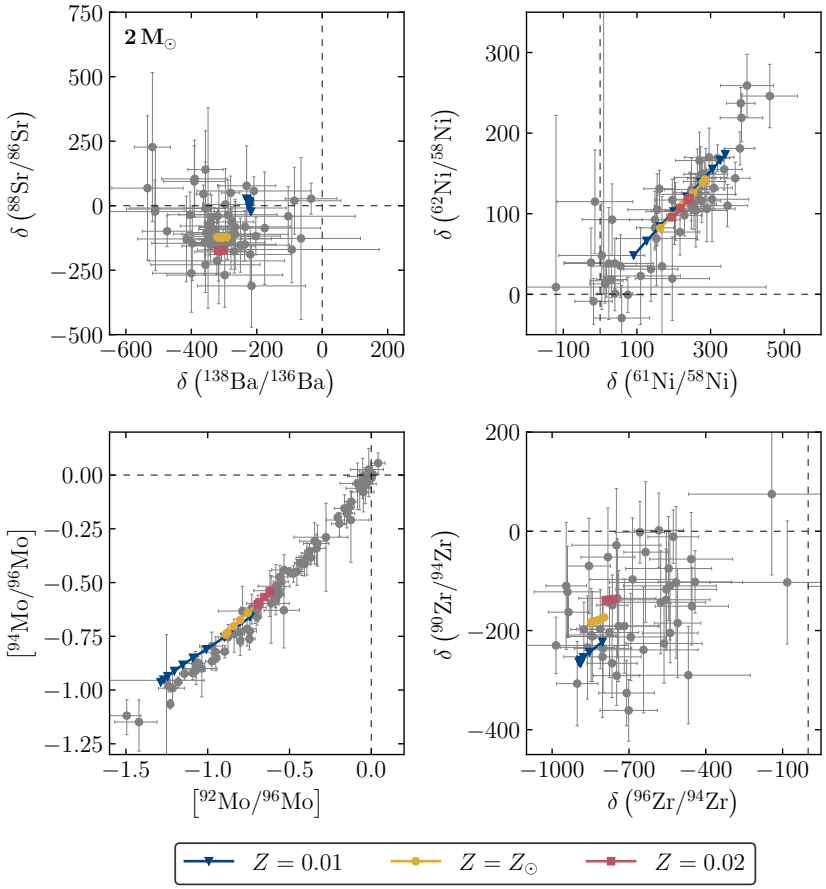

Figure 1. Comparison between FRUITY Magnetic 2 $M_{\odot}$ models at different metallicities and presolar grain isotopic ratios. Grain data are from Nicolussi et al. [157], Barzyk et al. [158], Liu et al. [159], Liu et al. [151,160], Trappitsch et al. [161], Stephan et al. [162], Stephan et al. [163].

The action of magnetic-buoyancy-mixing results in deep penetration of a few protons, so that, when H-burning restarts, almost all the protons are captured by ^{12}C, producing ^{13}C but a small amount of ^{14}N. Therefore, the ensuing ^{13}C pocket is quite extended and with a low and rather constant ^{13}C abundance (see Figure 2), as required to explain Sr–Ba grain data [144,164,165]. Conversely, the scarcity of ^{14}N substantially inhibits the synthesis of those isotopes whose nuclear production channel starts from nitrogen, including ^{19}F (see Section 4.2).

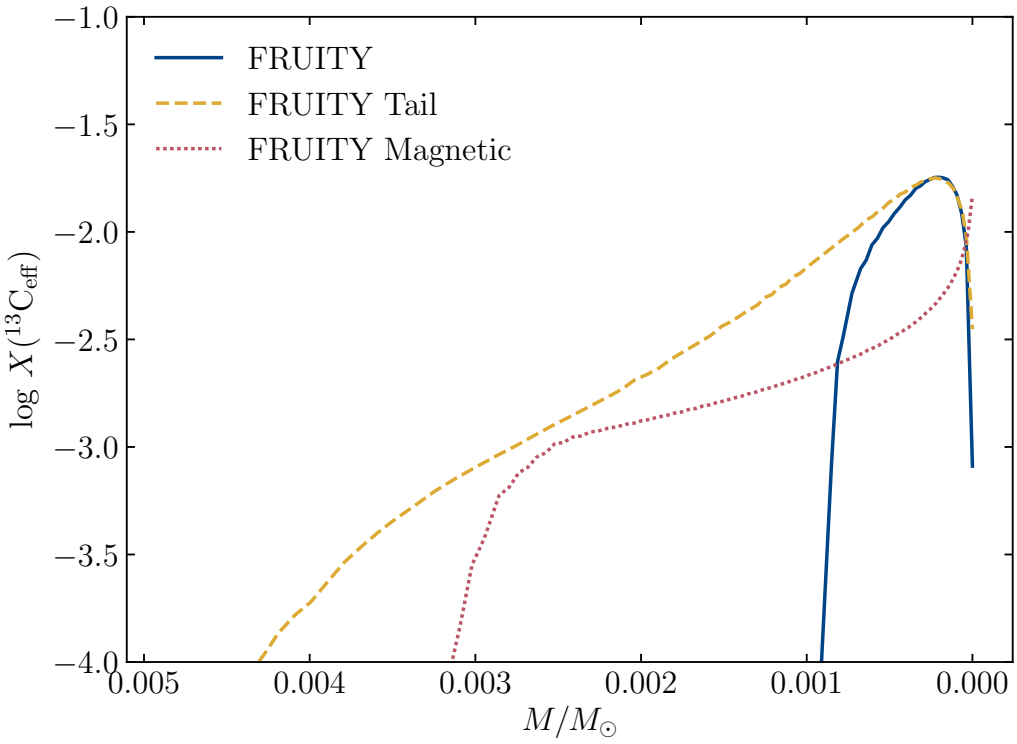

Figure 2. Effective ^{13}C in the ^{13}C pocket region for models with different physical prescriptions. The mass fraction of effective ^{13}C is defined as $X(^{13}C_{eff}) = X(^{13}C) - 13/14 \times X(^{14}N)$. Since ^{14}N is the most efficient neutron poison, the $X(^{13}C_{eff})$ quantifies the number of neutrons that will be released at following activation of the $^{13}C(\alpha, n)^{16}O$ reaction and therefore is a good estimator of the s-element production.

4.2. Fluorine Nucleosynthesis

One of the most fascinating subjects in nuclear astrophysics is the origin of fluorine in the Universe. While several sources are required to explain the galactic chemical evolution of fluorine abundance (see Grisoni et al. [166] and references therein), spectroscopic findings of photospheric [F/Fe] enhancements in intrinsic AGB carbon stars [167–171] and metal-poor extrinsic stars [171,172] provide the only direct observation of fluorine production. In AGB stars, starting from free neutrons and ^{14}N, the fluorine synthesis occurs via the reactions chain $^{14}N(n,p)^{14}C(\alpha,\gamma)^{18}O(p,\alpha)^{15}N(\alpha,\gamma)^{19}F$. Neutrons are made available through the activation of the $^{13}C(\alpha, n)^{16}O$ reaction. During the interpulse phase, neutrons are burnt along with the ^{14}N present in the He-intershell to synthesize ^{15}N, which is then consumed to create ^{19}F via $^{15}N(\alpha,\gamma)^{19}F$ reaction in the following convective TP [173–175]. ^{19}F is additionally produced from any secondary ^{13}C and ^{14}N left in H-burning ashes and from the eventual un-burnt ^{13}C in the pocket [12], that are engulfed in the convective shell generated by the TP. Fluorine is then brought by convective motions to the surface during the subsequent TDU. As a result, the ^{19}F envelope abundance should correlate with those of carbon and s-process elements (see Abia et al. [171] and references therein).

Compared to observational data for the F-enhancement trend with the metallicity, current theoretical predictions for low-mass AGB stars provide a good agreement [174,176].

When considering [F/s] ratios at close-to-solar metallicities, standard FRUITY models were shown to be able to reproduce the decreasing trend of [F/s] with the surface s-process enrichment. However, at lower metallicities they overestimate the fluorine production with respect to heavy elements [171,176]. Even FRUITY Tail models, despite the larger ^{13}C pockets leading to larger s-process surface enhancements, barely reach negative values for [F/Ba] and [F/La] observed in low-metallicity objects [171,172], pointing out that fluorine production needs to be further suppressed, without altering the s-process enrichment (see also Abia et al. [171]). Instead, FRUITY Magnetic models can effectively reproduce the observed spread for both [F/Ba] and [F/La] ratios as a function of the corresponding s-process enhancement (see Figure 3). As mentioned above, ^{19}F is primarily synthesized in AGB stars via a complex nuclear chain involving ^{14}N nuclei. In FRUITY Magnetic models, the low proton abundance resulting from the magnetic-buoyancy-induced mixing guarantees the production of a small amount of primary ^{14}N. As a consequence, this fluorine production channel is suppressed and, in those models, the fluorine envelope abundance is determined by the amount of secondary ^{14}N left behind by H-shell burning [49]. On the other hand, the extended ^{13}C pocket allows to achieve high s-enhancements that, coupled to low fluorine enhancements, put FRUITY Magnetic models in close agreement with observations in very metal-poor AGB stars.

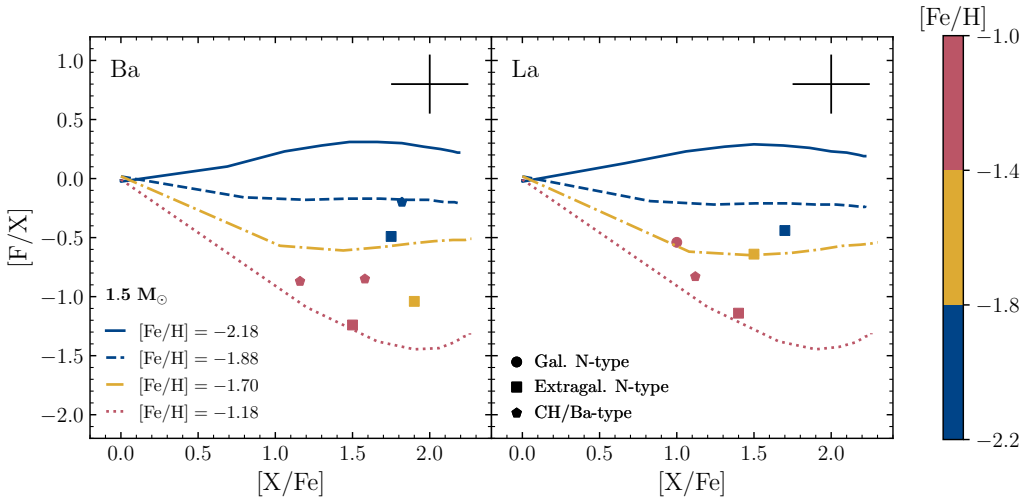

Figure 3. [F/X] against [X/Fe] for the sample stars with [Fe/H] ≤ -1.0. Symbols refer to three data groups: circles, galactic (N-type) carbon stars; squares, extragalactic carbon stars; pentagons, extrinsic CH/Ba stars. Data from Abia et al. [171], Lucatello et al. [172]. The lines are theoretical predictions for 1.5 $M_{\odot}$ AGB stars with low metallicity. Note that at these low metallicities, theoretical AGB models predict that the star becomes C-rich from the first TDU episodes. Data points and theoretical lines are color-coded by [Fe/H]. Typical error bars are indicated.

4.3. Stellar Yields and the Galactic Evolution of Yttrium Abundance

Stellar yields from AGB stars are crucial in building a galactic chemical evolution model. AGB yields from FRUITY models, when combined with yields for rotating massive star models from Limongi and Chieffi [177], successfully reproduce the solar distribution of s-process elements [143]. However, those yields are not able to explain the observed [Y/H] and [Y/Mg] abundance ratios of star clusters located in the inner galactic disk, that is, with Galactocentric distances $R_{GC} < 7$ kpc [178]. Instead, theoretical predictions on average agree with data for clusters located at larger radii. Analogous considerations apply for other literature s-process yields (see Casali et al. [178] and references therein). This points to the fact that clusters in the inner disk have a lower or equal yttrium abundance with respect to clusters located at higher R_{GC} at the same age. To reproduce the observed trends, Casali et al. [178] adopted a set of empirical yields in which the production of Y at high metallicity is significantly lowered (by a factor of ten). This suggests that current AGB models overestimate the yttrium yield trend with the metallicity because the neutron-to-

seed ratio attained in those models is likely excessive, as also indicated by the comparison with isotope ratios of heavy elements measured in presolar SiC grains [179,180]. Conversely, FRUITY models accounting for mixing triggered by magnetic fields were shown to provide a good match to grain data (see Section 4.1) and reach milder neutron densities than standard FRUITY models at close-to-solar metallicities.

The yttrium and barium net yields for a 2 $M_{\odot}$ star as a function of [Fe/H] both for FRUITY Standard and FRUITY Magnetic models are shown in Figure 4. The two sets are markedly different due to different attained neutron-to-seed ratios. The latter is determined by the number of free neutrons, that are of primary origin, and the number of iron nuclei as seeds for the neutron captures, which is instead a secondary-like quantity that depends on the metallicity. Overall, magnetic models present fewer neutrons and so a lower neutron-to-seed ratio. At low metallicities, this implies that the neutron fluxes are sufficiently high to robustly produce Y but not to saturate the first s-process peak and move to the second peak, so efficiently producing Ba. On the contrary, moving at higher metallicities, the net Y production of magnetic models drops faster than standard FRUITY models. The decrease is less evident for the Ba yields. Such differences in the net yields have a decisive impact in a galactic chemical evolution (GCE) modeling of the inner Galactic disk, where super-solar metallicity is reached. Including the set of FRUITY Magnetic stellar yields in a GCE model, it was shown that it is possible to reproduce the almost constant trend of [Y/H] versus age while adopting standard FRUITY yields would result in a net increase of [Y/H] in the inner disk regions (that is not observed; see [149]). Similar outcomes were also obtained when considering Zr, Ba, La, and Ce trends [149]. In this framework, present FRUITY Magnetic models offer a theoretical explanation of the behavior of slow neutron-capture elements in the inner Galactic disk.

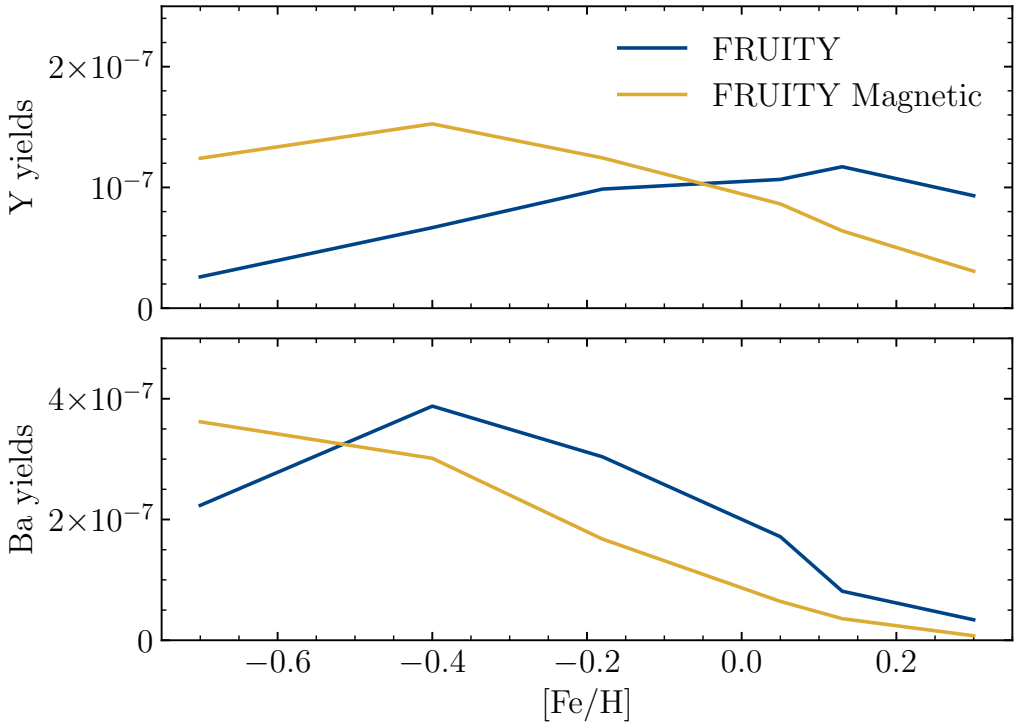

Figure 4. Net yttrium (top panel) and net barium (bottom panel) yields as a function of [Fe/H] for a 2 $M_{\odot}$ AGB star as predicted by FRUITY and FRUITY Magnetic models.

5. Summary and Outlook

Significant improvements in understanding the evolution and nucleosynthesis of AGB stars have been made in recent years. One of the remaining unknowns concerns the physical mechanism responsible for the formation of the ^{13}C neutron source in these stars. Several additional transport processes have been invoked and accordingly included

in stellar evolution codes. Among them, the mixing induced by magnetic buoyancy of material in the He-rich regions to the envelope has shown to induce the development of rather extended ^{13}C pockets. Post-process models adopting such ^{13}C-reservoirs are able to reproduce many observational constraints.

In this review, we have discussed a new series of FRUITY models accounting for the magnetic-buoyancy-induced mixing, which is now included in the FUNS evolutionary code, along with the latest available input physics data. Once properly calibrated, FRUITY Magnetic models of 2 $M_{\odot}$ and close-to-solar metallicity provide a very good match to most of the isotope ratios measured in presolar SiC grains. The peculiar proton profile in these models leads to the generation of extended ^{13}C pockets moderately-rich in ^{13}C and with a small amount of ^{14}N. This has various implications. The first is a relatively low ^{19}F envelope abundance, accompanied by a significant production of s-process nuclei. In turn, this results in high surface s-process enrichment at low metallicities that, combined with mild fluorine enhancements, pose magnetic FRUITY models in fair agreement with observations for Galactic and extragalactic AGB stars. Instead, models with solar and super-solar metallicity, substantially favor the production of light s-process elements against heavy ones. Therefore, yields from magnetic FRUITY models for elements like yttrium show a decreasing metallicity trend, as required by GCE models reproducing the s-process elements behavior in galactic open clusters.

These results add to the evidence that the present calibration of the parameters describing the magnetic-buoyancy-induced mixing adopted in FRUITY models is robust. Nonetheless, additional pieces of evidence, based both on further comparisons with intrinsic and extrinsic objects, as barium stars and post-AGB stars, and multidimensional magnetohydrodynamic simulations are needed for a definitive claim.

Funding: This work was supported by the German-Israeli Foundation (GIF No. I-1500-303.7/2019).

Institutional Review Board Statement: Not applicable.

Informed Consent Statement: Not applicable.

Data Availability Statement: Presolar grain data are from the Presolar Grain Database of the Laboratory for Space at Washington University in St. Louis, USA (https://presolar.physics.wustl.edu/presolar-grain-database (accessed on 2 December 2021)).

Acknowledgments: The authors thank S. Cristallo for useful discussions and for reading the manuscript.

Conflicts of Interest: The authors declare no conflict of interest.

References

1. Käppeler, F.; Gallino, R.; Bisterzo, S.; Aoki, W. The s process: Nuclear physics, stellar models, and observations. *Rev. Mod. Phys.* **2011**, *83*, 157–194. [CrossRef]
2. Cowan, J.J.; Sneden, C.; Lawler, J.E.; Aprahamian, A.; Wiescher, M.; Langanke, K.; Martínez-Pinedo, G.; Thielemann, F.K. Origin of the heaviest elements: The rapid neutron-capture process. *Rev. Mod. Phys.* **2021**, *93*, 015002. [CrossRef]
3. Burbidge, E.M.; Burbidge, G.R.; Fowler, W.A.; Hoyle, F. Synthesis of the Elements in Stars. *Rev. Mod. Phys.* **1957**, *29*, 547–650. [CrossRef]
4. Busso, M.; Gallino, R.; Wasserburg, G.J. Nucleosynthesis in Asymptotic Giant Branch Stars: Relevance for Galactic Enrichment and Solar System Formation. *Annu. Rev. Astron. Astrophys.* **1999**, *37*, 239–309. [CrossRef]
5. Raiteri, C.M.; Gallino, R.; Busso, M.; Neuberger, D.; Käppeler, F. The Weak s-Component and Nucleosynthesis in Massive Stars. *Astrophys. J.* **1993**, *419*, 207. [CrossRef]
6. Karakas, A.I.; Lattanzio, J.C. The Dawes Review 2: Nucleosynthesis and Stellar Yields of Low- and Intermediate-Mass Single Stars. *Publ. Astron. Soc. Aust.* **2014**, *31*, e030. [CrossRef]
7. Cristallo, S.; Straniero, O.; Piersanti, L.; Gobrecht, D. Evolution, Nucleosynthesis, and Yields of AGB Stars at Different Metallicities. III. Intermediate-mass Models, Revised Low-mass Models, and the ph-FRUITY Interface. *Astrophys. J. Suppl.* **2015**, *219*, 40. [CrossRef]
8. Straniero, O.; Gallino, R.; Busso, M.; Chiefei, A.; Raiteri, C.M.; Limongi, M.; Salaris, M. Radiative 13C Burning in Asymptotic Giant Branch Stars and *s*-Processing. *Astrophys. J. Lett.* **1995**, *440*, L85. [CrossRef]
9. Gallino, R.; Arlandini, C.; Busso, M.; Lugaro, M.; Travaglio, C.; Straniero, O.; Chieffi, A.; Limongi, M. Evolution and Nucleosynthesis in Low-Mass Asymptotic Giant Branch Stars. II. Neutron Capture and the S-Process. *Astrophys. J.* **1998**, *497*, 388–403. [CrossRef]

10. Busso, M.; Gallino, R.; Lambert, D.L.; Travaglio, C.; Smith, V.V. Nucleosynthesis and Mixing on the Asymptotic Giant Branch. III. Predicted and Observed s-Process Abundances. *Astrophys. J.* **2001**, *557*, 802–821. [CrossRef]
11. Cox, J.P.; Giuli, R.T. *Principles of Stellar Structure*; Gordon and Breach: New York, NY, USA, 1968.
12. Cristallo, S.; Straniero, O.; Gallino, R.; Piersanti, L.; Domínguez, I.; Lederer, M.T. Evolution, Nucleosynthesis, and Yields of Low-Mass Asymptotic Giant Branch Stars at Different Metallicities. *Astrophys. J.* **2009**, *696*, 797–820. [CrossRef]
13. Trippella, O.; Busso, M.; Palmerini, S.; Maiorca, E.; Nucci, M.C. *s*-Processing in AGB Stars Revisited. II. Enhanced 13C Production through MHD-induced Mixing. *Astrophys. J.* **2016**, *818*, 125. [CrossRef]
14. Herwig, F.; Bloecker, T.; Schoenberner, D.; El Eid, M. Stellar evolution of low and intermediate-mass stars. IV. Hydrodynamically-based overshoot and nucleosynthesis in AGB stars. *Astron. Astrophys.* **1997**, *324*, L81–L84.
15. Frost, C.A.; Lattanzio, J.C. On the Numerical Treatment and Dependence of the Third Dredge-up Phenomenon. *Astrophys. J.* **1996**, *473*, 383. [CrossRef]
16. Herwig, F. The evolution of AGB stars with convective overshoot. *Astron. Astrophys.* **2000**, *360*, 952–968.
17. Straniero, O.; Gallino, R.; Cristallo, S. *s* process in low-mass asymptotic giant branch stars. *Nucl. Phys. A* **2006**, *777*, 311–339. [CrossRef]
18. Goriely, S.; Siess, L. Sensitivity of the s-process nucleosynthesis in AGB stars to the overshoot model. *Astron. Astrophys.* **2018**, *609*, A29. [CrossRef]
19. Freytag, B.; Ludwig, H.G.; Steffen, M. Hydrodynamical models of stellar convection. The role of overshoot in DA white dwarfs, A-type stars, and the Sun. *Astron. Astrophys.* **1996**, *313*, 497–516.
20. Herwig, F.; Freytag, B.; Fuchs, T.; Hansen, J.P.; Hueckstaedt, R.M.; Porter, D.H.; Timmes, F.X.; Woodward, P.R. Convective and Non-Convective Mixing in AGB Stars. *arXiv* **2007**, arXiv:0709.0197.
21. Battino, U.; Pignatari, M.; Ritter, C.; Herwig, F.; Denisenkov, P.; Den Hartogh, J.W.; Trappitsch, R.; Hirschi, R.; Freytag, B.; Thielemann, F.; et al. Application of a Theory and Simulation-based Convective Boundary Mixing Model for AGB Star Evolution and Nucleosynthesis. *Astrophys. J.* **2016**, *827*, 30. [CrossRef]
22. Battino, U.; Tattersall, A.; Lederer-Woods, C.; Herwig, F.; Denissenkov, P.; Hirschi, R.; Trappitsch, R.; den Hartogh, J.W.; Pignatari, M.; NuGrid Collaboration. NuGrid stellar data set-III. Updated low-mass AGB models and s-process nucleosynthesis with metallicities Z= 0.01, Z = 0.02, and Z = 0.03. *Month. Not. R. Astron. Soc.* **2019**, *489*, 1082–1098. [CrossRef]
23. Denissenkov, P.A.; Tout, C.A. Partial mixing and formation of the ^{13}C pocket by internal gravity waves in asymptotic giant branch stars. *Month. Not. R. Astron. Soc.* **2003**, *340*, 722–732. [CrossRef]
24. Maeder, A. *Physics, Formation and Evolution of Rotating Stars*; Springer: Berlin/Heidelberg, Germany, 2009.
25. Aerts, C. Probing the interior physics of stars through asteroseismology. *arXiv* **2019**, arXiv:1912.12300.
26. Langer, N.; Heger, A.; Wellstein, S.; Herwig, F. Mixing and nucleosynthesis in rotating TP-AGB stars. *Astron. Astrophys.* **1999**, *346*, L37–L40.
27. Herwig, F.; Langer, N.; Lugaro, M. The s-Process in Rotating Asymptotic Giant Branch Stars. *Astrophys. J.* **2003**, *593*, 1056–1073. [CrossRef]
28. Siess, L.; Goriely, S.; Langer, N. Nucleosynthesis of s-elements in rotating AGB stars. *Astron. Astrophys.* **2004**, *415*, 1089–1097. [CrossRef]
29. Piersanti, L.; Cristallo, S.; Straniero, O. The Effects of Rotation on s-process Nucleosynthesis in Asymptotic Giant Branch Stars. *Astrophys. J.* **2013**, *774*, 98. [CrossRef]
30. den Hartogh, J.W.; Hirschi, R.; Lugaro, M.; Doherty, C.L.; Battino, U.; Herwig, F.; Pignatari, M.; Eggenberger, P. The s process in rotating low-mass AGB stars. Nucleosynthesis calculations in models matching asteroseismic constraints. *Astron. Astrophys.* **2019**, *629*, A123. [CrossRef]
31. Braithwaite, J.; Spruit, H.C. Magnetic fields in non-convective regions of stars. *R. Soc. Open Sci.* **2017**, *4*, 160271. [CrossRef] [PubMed]
32. Busso, M.; Wasserburg, G.J.; Nollett, K.M.; Calandra, A. Can Extra Mixing in RGB and AGB Stars Be Attributed to Magnetic Mechanisms? *Astrophys. J.* **2007**, *671*, 802–810. [CrossRef]
33. Aerts, C.; Mathis, S.; Rogers, T.M. Angular Momentum Transport in Stellar Interiors. *Annu. Rev. Astron. Astrophys.* **2019**, *57*, 35–78. [CrossRef]
34. Nucci, M.C.; Busso, M. Magnetohydrodynamics and Deep Mixing in Evolved Stars. I. Two- and Three-dimensional Analytical Models for the Asymptotic Giant Branch. *Astrophys. J.* **2014**, *787*, 141. [CrossRef]
35. Parker, E.N. The Hydrodynamic Theory of Solar Corpuscular Radiation and Stellar Winds. *Astrophys. J.* **1960**, *132*, 821. [CrossRef]
36. Spruit, H.C. Differential rotation and magnetic fields in stellar interiors. *Astron. Astrophys.* **1999**, *349*, 189–202.
37. Schuessler, M. On buoyant magnetic flux tube in the solar convection zone. *Astron. Astrophys.* **1977**, *56*, 439–442.
38. Trippella, O.; Busso, M.; Maiorca, E.; Käppeler, F.; Palmerini, S. *s*-Processing in AGB Stars Revisited. I. Does the Main Component Constrain the Neutron Source in the ^{13}C Pocket? *Astrophys. J.* **2014**, *787*, 41. [CrossRef]
39. Vescovi, D.; Busso, M.; Palmerini, S.; Trippella, O.; Cristallo, S.; Piersanti, L.; Chieffi, A.; Limongi, M.; Hoppe, P.; Kratz, K. -L. On the Origin of Early Solar System Radioactivities: Problems with the Asymptotic Giant Branch and Massive Star Scenarios. *Astrophys. J.* **2018**, *863*, 115. [CrossRef]
40. Ventura, P.; D'Antona, F.; Mazzitelli, I.; Gratton, R. Predictions for Self-Pollution in Globular Cluster Stars. *Astrophys. J. Lett.* **2001**, *550*, L65–L69. [CrossRef]

41. Herwig, F. Evolution and Yields of Extremely Metal-poor Intermediate-Mass Stars. *Astrophys. J. Suppl.* **2004**, *155*, 651–666. [CrossRef]
42. Karakas, A.; Lattanzio, J.C. Stellar Models and Yields of Asymptotic Giant Branch Stars. *Publ. Astron. Soc. Aust.* **2007**, *24*, 103–117. [CrossRef]
43. Cristallo, S.; Piersanti, L.; Straniero, O.; Gallino, R.; Domínguez, I.; Abia, C.; Di Rico, G.; Quintini, M.; Bisterzo, S. Evolution, Nucleosynthesis, and Yields of Low-mass Asymptotic Giant Branch Stars at Different Metallicities. II. The FRUITY Database. *Astrophys. J. Suppl.* **2011**, *197*, 17. [CrossRef]
44. Ritter, C.; Herwig, F.; Jones, S.; Pignatari, M.; Fryer, C.; Hirschi, R. NuGrid stellar data set-II. Stellar yields from H to Bi for stellar models with M_{ZAMS} = 1–25 $M_{\odot}$ and Z = 0.0001–0.02. *Month. Not. R. Astron. Soc.* **2018**, *480*, 538–571. [CrossRef]
45. Rogers, F.J.; Swenson, F.J.; Iglesias, C.A. OPAL Equation-of-State Tables for Astrophysical Applications. *Astrophys. J.* **1996**, *456*, 902. [CrossRef]
46. Straniero, O. A tabulation of thermodynamical properties of fully ionized matter in stellar interiors. *Astron. Astrophys. Suppl.* **1988**, *76*, 157–184.
47. Prada Moroni, P.G.; Straniero, O. Calibration of White Dwarf Cooling Sequences: Theoretical Uncertainty. *Astrophys. J.* **2002**, *581*, 585–597. [CrossRef]
48. Lodders, K. Relative Atomic Solar System Abundances, Mass Fractions, and Atomic Masses of the Elements and Their Isotopes, Composition of the Solar Photosphere, and Compositions of the Major Chondritic Meteorite Groups. *Space Sci. Rev.* **2021**, *217*, 44. [CrossRef]
49. Vescovi, D.; Cristallo, S.; Palmerini, S.; Abia, C.; Busso, M. Magnetic-buoyancy-induced mixing in AGB Stars: fluorine nucleosynthesis at different metallicities. *arXiv* **2021**, arXiv:2106.08241.
50. Iglesias, C.A.; Rogers, F.J. Updated Opal Opacities. *Astrophys. J.* **1996**, *464*, 943. [CrossRef]
51. Potekhin, A.Y.; Baiko, D.A.; Haensel, P.; Yakovlev, D.G. Transport properties of degenerate electrons in neutron star envelopes and white dwarf cores. *Astron. Astrophys.* **1999**, *346*, 345–353.
52. Shternin, P.S.; Yakovlev, D.G. Electron thermal conductivity owing to collisions between degenerate electrons. *Phys. Rev. D* **2006**, *74*, 043004. [CrossRef]
53. Marigo, P.; Aringer, B. Low-temperature gas opacity. ÆSOPUS: a versatile and quick computational tool. *Astron. Astrophys.* **2009**, *508*, 1539–1569. [CrossRef]
54. Höfner, S.; Olofsson, H. Mass loss of stars on the asymptotic giant branch. Mechanisms, models and measurements. *Astron. Astrophys. Rev.* **2018**, *26*, 1. [CrossRef]
55. Ventura, P.; Karakas, A.I.; Dell'Agli, F.; Boyer, M.L.; García-Hernández, D.A.; Di Criscienzo, M.; Schneider, R. The Large Magellanic Cloud as a laboratory for hot bottom burning in massive asymptotic giant branch stars. *Month. Not. R. Astron. Soc.* **2015**, *450*, 3181–3190. [CrossRef]
56. Vassiliadis, E.; Wood, P.R. Evolution of Low- and Intermediate-Mass Stars to the End of the Asymptotic Giant Branch with Mass Loss. *Astrophys. J.* **1993**, *413*, 641. [CrossRef]
57. Whitelock, P.A.; Feast, M.W.; van Loon, J.T.; Zijlstra, A.A. Obscured asymptotic giant branch variables in the Large Magellanic Cloud and the period-luminosity relation. *Month. Not. R. Astron. Soc.* **2003**, *342*, 86–104. [CrossRef]
58. Abia, C.; de Laverny, P.; Cristallo, S.; Kordopatis, G.; Straniero, O. Properties of carbon stars in the solar neighbourhood based on Gaia DR2 astrometry. *Astron. Astrophys.* **2020**, *633*, A135. [CrossRef]
59. Buzzoni, A.; Patelli, L.; Bellazzini, M.; Pecci, F.F.; Oliva, E. Bolometric correction and spectral energy distribution of cool stars in Galactic clusters. *Month. Not. R. Astron. Soc.* **2010**, *403*, 1592–1610. [CrossRef]
60. Dillmann, I.; Plag, R.; Käppeler, F.; Rauscher, T. EFNUDAT Fast Neutrons-Scientific Workshop on Neutron Measurements, Theory & Applications. JRC-IRMM. 2009. Available online: http://www.kadonis.org (accessed on 28 August 2009).
61. Rugel, G.; Faestermann, T.; Knie, K.; Korschinek, G.; Poutivtsev, M.; Schumann, D.; Kivel, N.; Günther-Leopold, I.; Weinreich, R.; Wohlmuther, M. New Measurement of the Fe60 Half-Life. *Phys. Rev. L* **2009**, *103*, 072502. [CrossRef] [PubMed]
62. Uberseder, E.; Reifarth, R.; Schumann, D.; Dillmann, I.; Pardo, C.D.; Görres, J.; Heil, M.; Käppeler, F.; Marganiec, J.; Neuhausen, J.; et al. Measurement of the ^{60}Fe$(n,\gamma)^{61}$Fe cross-section at Stellar Temperatures. *Phys. Rev. Lett.* **2009**, *102*, 151101. [CrossRef] [PubMed]
63. Simonucci, S.; Taioli, S.; Palmerini, S.; Busso, M. Theoretical Estimates of Stellar e—Captures. I. The Half-life of 7Be in Evolved Stars. *Astrophys. J.* **2013**, *764*, 118. [CrossRef]
64. Vescovi, D.; Piersanti, L.; Cristallo, S.; Busso, M.; Vissani, F.; Palmerini, S.; Simonucci, S.; Taioli, S. Effects of a revised ^{7}Be e^{-}-capture rate on solar neutrino fluxes. *Astron. Astrophys.* **2019**, *623*, A126. [CrossRef]
65. Reifarth, R.; Erbacher, P.; Fiebiger, S.; Göbel, K.; Heftrich, T.; Heil, M.; Käppeler, F.; Klapper, N.; Kurtulgil, D.; Langer, C.; et al. Neutron-induced cross-sections. From raw data to astrophysical rates. *Eur. Phys. J. Plus* **2018**, *133*, 424. [CrossRef]
66. Vescovi, D.; Reifarth, R. *s*-Processing in Asymptotic Giant Branch Stars in the Light of Revised Neutron-Capture cross-sections. *Universe* **2021**, *7*, 239. [CrossRef]
67. Lamia, L.; Spitaleri, C.; La Cognata, M.; Palmerini, S.; Pizzone, R.G. Recent evaluation of the ^{7}Li(p, α)^{4}He reaction rate at astrophysical energies via the Trojan Horse method. *Astron. Astrophys.* **2012**, *541*, A158. [CrossRef]
68. Cesaratto, J.M.; Champagne, A.E.; Buckner, M.Q.; Clegg, T.B.; Daigle, S.; Howard, C.; Iliadis, C.; Longland, R.; Newton, J.R.; Oginni, B.M. Measurement of the $E_r^{c.m.} = 138$ keV resonance in the ^{23}Na$(p,\gamma)^{24}$Mg reaction and the abundance of sodium in AGB stars. *Phys. Rev. C* **2013**, *88*, 065806. [CrossRef]

69. Costantini, H.; deBoer, R.J.; Azuma, R.E.; Couder, M.; Görres, J.; Hammer, J.W.; LeBlanc, P.J.; Lee, H.Y.; O'Brien, S.; Palumbo, A.; et al. $^{16}O(\alpha,\gamma)^{20}Ne$ *S* factor: Measurements and *R*-matrix analysis. *Phys. Rev. C* **2010**, *82*, 035802. [CrossRef]
70. LeBlanc, P.J.; Imbriani, G.; Görres, J.; Junker, M.; Azuma, R.; Beard, M.; Bemmerer, D.; Best, A.; Broggini, C.; Caciolli, A.; et al. Constraining the *S* factor of $^{15}N(p,\gamma)^{16}O$ at astrophysical energies. *Phys. Rev. C* **2010**, *82*, 055804. [CrossRef]
71. Iliadis, C.; Longland, R.; Champagne, A.E.; Coc, A.; Fitzgerald, R. Charged-particle thermonuclear reaction rates: II. Tables and graphs of reaction rates and probability density functions. *Nucl. Phys. A* **2010**, *841*, 31–250. [CrossRef]
72. Di Leva, A.; Scott, D.A.; Caciolli, A.; Formicola, A.; Strieder, F.; Aliotta, M.; Anders, M.; Bemmerer, D.; Broggini, C.; Corvisiero, P.; et al. Underground study of the $^{17}O(p,\gamma)^{18}F$ reaction relevant for explosive hydrogen burning. *Phys. Rev. C* **2014**, *89*, 015803. [CrossRef]
73. Adsley, P.; Battino, U.; Best, A.; Caciolli, A.; Guglielmetti, A.; Imbriani, G.; Jayatissa, H.; La Cognata, M.; Lamia, L.; Masha, E.; et al. Reevaluation of the $^{22}Ne(\alpha,\gamma)^{26}Mg$ and $^{22}Ne(\alpha,n)^{25}Mg$ reaction rates. *Phys. Rev. C* **2021**, *103*, 015805. [CrossRef]
74. Bruno, C.G.; Scott, D.A.; Aliotta, M.; Formicola, A.; Best, A.; Boeltzig, A.; Bemmerer, D.; Broggini, C.; Caciolli, A.; Cavanna, F.; et al. Improved Direct Measurement of the 64.5 keV Resonance Strength in the $^{17}O(p,\alpha)^{14}N$ Reaction at LUNA. *Phys. Rev. Lett.* **2016**, *117*, 142502. [CrossRef]
75. Straniero, O.; Imbriani, G.; Strieder, F.; Bemmerer, D.; Broggini, C.; Caciolli, A.; Corvisiero, P.; Costantini, H.; Cristallo, S.; DiLeva, A.; et al. Impact of a Revised $^{25}Mg(p,\gamma)^{26}Al$ Reaction Rate on the Operation of the Mg-Al Cycle. *Astrophys. J.* **2013**, *763*, 100. [CrossRef]
76. Buckner, M.Q.; Iliadis, C.; Kelly, K.J.; Downen, L.N.; Champagne, A.E.; Cesaratto, J.M.; Howard, C.; Longland, R. High-intensity-beam study of $^{17}O(p,\gamma)^{18}F$ and thermonuclear reaction rates for $^{17}O+p$. *Phys. Rev. C* **2015**, *91*, 015812. [CrossRef]
77. Best, A.; Pantaleo, F.R.; Boeltzig, A.; Imbriani, G.; Aliotta, M.; Balibrea-Correa, J.; Bemmerer, D.; Broggini, C.; Bruno, C.G.; Buompane, R.; et al. cross-section of the reaction $^{18}O(p,\gamma)^{19}F$ at astrophysical energies: The 90 keV resonance and the direct capture component. *Phys. Lett. B* **2019**, *797*, 134900. [CrossRef]
78. Bruno, C.G.; Aliotta, M.; Descouvemont, P.; Best, A.; Davinson, T.; Bemmerer, D.; Boeltzig, A.; Broggini, C.; Caciolli, A.; Cavanna, F.; et al. Improved astrophysical rate for the $^{18}O(p,\alpha)^{15}N$ reaction by underground measurements. *Phys. Lett. B* **2019**, *790*, 237–242. [CrossRef]
79. Best, A.; Beard, M.; Görres, J.; Couder, M.; deBoer, R.; Falahat, S.; Güray, R.T.; Kontos, A.; Kratz, K.-L.; LeBlanc, P.J.; et al. Measurement of the reaction $^{17}O(\alpha,n)^{20}Ne$ and its impact on the *s* process in massive stars. *Phys. Rev. C* **2013**, *87*, 045805. [CrossRef]
80. Indelicato, I.; La Cognata, M.; Spitaleri, C.; Burjan, V.; Cherubini, S.; Gulino, M.; Hayakawa, S.; Hons, Z.; Kroha, V.; Lamia, L.; et al. New Improved Indirect Measurement of the $^{19}F(p,\alpha)^{16}O$ Reaction at Energies of Astrophysical Relevance. *Astrophys. J.* **2017**, *845*, 19. [CrossRef]
81. Lamia, L.; Spitaleri, C.; Tognelli, E.; Degl'Innocenti, S.; Pizzone, R.G.; Prada Moroni, P.G. Astrophysical Impact of the Updated $^{9}Be(p,\alpha)^{6}Li$ and $^{10}B(p,\alpha)^{7}Be$ Reaction Rates As Deduced By THM. *Astrophys. J.* **2015**, *811*, 99. [CrossRef]
82. Best, A.; Falahat, S.; Görres, J.; Couder, M.; deBoer, R.; Güray, R.T.; Kontos, A.; Kratz, K.L.; LeBlanc, P.J.; Li, Q.; et al. Measurement of the reaction $^{18}O(\alpha,n)^{21}Ne$. *Phys. Rev. C* **2013**, *87*, 045806. [CrossRef]
83. Angulo, C.; Arnould, M.; Rayet, M.; Descouvemont, P.; Baye, D.; Leclercq-Willain, C.; Coc, A.; Barhoumi, S.; Aguer, P.; Rolfs, C.; et al. A compilation of charged-particle induced thermonuclear reaction rates. *Nucl. Phys. A* **1999**, *656*, 3–183. [CrossRef]
84. D'Agata, G.; Pizzone, R.G.; La Cognata, M.; Indelicato, I.; Spitaleri, C.; Palmerini, S.; Trippella, O.; Vescovi, D.; Blagus, S.; Cherubini, S.; et al. The $^{19}F(\alpha,p)^{22}Ne$ Reaction at Energies of Astrophysical Relevance by Means of the Trojan Horse Method and Its Implications in AGB Stars. *Astrophys. J.* **2018**, *860*, 61. [CrossRef]
85. Kunz, R.; Fey, M.; Jaeger, M.; Mayer, A.; Hammer, J.W.; Staudt, G.; Harissopulos, S.; Paradellis, T. Astrophysical Reaction Rate of $^{12}C(\alpha,\gamma)^{16}O$. *Astrophys. J.* **2002**, *567*, 643–650. doi: 10.1086/338384. [CrossRef]
86. Ciani, G.F.; Csedreki, L.; Rapagnani, D.; Aliotta, M.; Balibrea-Correa, J.; Barile, F.; Bemmerer, D.; Best, A.; Boeltzig, A.; Broggini,C.; et al. Direct Measurement of the $^{13}C(\alpha,n)^{16}O$ cross-section into the *s*-Process Gamow Peak. *Phys. Rev. Lett.* **2021**, *127*, 152701. [CrossRef] [PubMed]
87. Depalo, R.; Cavanna, F.; Aliotta, M.; Anders, M.; Bemmerer, D.; Best, A.; Boeltzig, A.; Broggini, C.; Bruno, C.G.; Caciolli, A.; et al. Direct measurement of low-energy $^{22}Ne(p,\gamma)^{23}Na$ resonances. *Phys. Rev. C* **2016**, *94*, 055804. [CrossRef]
88. Johnson, E.D.; Rogachev, G.V.; Mitchell, J.; Miller, L.; Kemper, K.W. C14(α,γ) reaction rate. *Phys. Rev. C* **2009**, *80*, 045805. [CrossRef]
89. Sallaska, A.L.; Iliadis, C.; Champange, A.E.; Goriely, S.; Starrfield, S.; Timmes, F.X. STARLIB: A Next-generation Reaction-rate Library for Nuclear Astrophysics. *Astrophys. J. Suppl.* **2013**, *207*, 18. [CrossRef]
90. Wallner, A.; Bichler, M.; Buczak, K.; Dillmann, I.; Käppeler, F.; Karakas, A.; Lederer, C.; Lugaro, M.; Mair, K.; Mengoni, A.; et al. Accelerator mass spectrometry measurements of the $^{13}C(n,\gamma)^{14}C$ and $^{14}N(n,p)^{14}C$ cross-sections. *Phys. Rev. C* **2016**, *93*, 045803. [CrossRef]
91. Marganiec, J.; Dillmann, I.; Pardo, C.D.; Käppeler, F.; Reifarth, R.; Gallino, R.; Pignatari, M.; Grabmayr, P. Neutron capture cross-sections of Ge74, Ge76, and As75 at 25 keV. *Phys. Rev. C* **2009**, *79*, 065802. [CrossRef]
92. Roig, O.; Jandel, M.; Méot, V.; Bond, E.M.; Bredeweg, T.A.; Couture, A.J.; Haight, R.C.; Keksis, A.L.; Rundberg, R.S.; Ullmann, J.L.; et al. Radiative neutron capture cross-sections on ^{176}Lu at DANCE. *Phys. Rev. C* **2016**, *93*, 034602. [CrossRef]

93. Heil, M.; Käppeler, F.; Uberseder, E.; Gallino, R.; Bisterzo, S.; Pignatari, M. Stellar (n,γ) cross-sections for Br and Rb: Matching the weak and main s-process components. *Phys. Rev. C* **2008**, *78*, 025802. [CrossRef]
94. Vockenhuber, C.; Dillmann, I.; Heil, M.; Käppeler, F.; Winckler, N.; Kutschera, W.; Wallner, A.; Bichler, M.; Dababneh, S.; Bisterzo, S.; et al. Stellar (n,γ) cross-sections of Hf174 and radioactive Hf182. *Phys. Rev. C* **2007**, *75*, 015804. [CrossRef]
95. Guardo, G.L.; Spitaleri, C.; Lamia, L.; Gulino, M.; La Cognata, M.; Tang, X.; deBoer, R.; Fang, X.; Goldberg, V.; Mrazek, J.; et al. Assessing the near threshold cross-section of the ^{17}O(n ,α)^{14}C reaction by means of the Trojan horse method. *Phys. Rev. C* **2017**, *95*, 025807. [CrossRef]
96. Wisshak, K.; Voss, F.; Käppeler, F.; Kazakov, L.; Bečvář, F.; Krtička, M.; Gallino, R.; Pignatari, M. Fast neutron capture on the Hf isotopes: cross-sections, isomer production, and stellar aspects. *Phys. Rev. C* **2006**, *73*, 045807. [CrossRef]
97. Uberseder, E.; Heil, M.; Käppeler, F.; Görres, J.; Wiescher, M. New measurements of the F19(n,γ)F20 cross section and their implications for the stellar reaction rate. *Phys. Rev. C* **2007**, *75*, 035801. [CrossRef]
98. Tessler, M.; Zappala, J.; Cristallo, S.; Roberti, L.; Paul, M.; Halfon, S.; Heftrich, T.; Jiang, W.; Kijel, D.; Kreisel, A.; et al. Stellar *s*-process neutron capture cross-sections on ^{78,80,84,86}Kr determined via activation, atom trap trace analysis, and decay counting. *Phys. Rev. C* **2021**, *104*, 015806. [CrossRef]
99. Heil, M.; Plag, R.; Uberseder, E.; Gallino, R.; Bisterzo, S.; Juseviciute, A.; Käppeler, F.; Lederer, C.; Mengoni, A.; Pignatari, M. Stellar neutron capture cross-sections of ^{20,21,22}Ne. *Phys. Rev. C* **2014**, *90*, 045804. [CrossRef]
100. Uberseder, E.; Heil, M.; Käppeler, F.; Lederer, C.; Mengoni, A.; Bisterzo, S.; Pignatari, M.; Wiescher, M. Stellar (n,γ) cross-sections of ^{23}Na. *Phys. Rev. C* **2017**, *95*, 025803. [CrossRef]
101. Massimi, C.; Koehler, P.; Bisterzo, S.; Colonna, N.; Gallino, R.; Gunsing, F.; Käppeler, F.; Lorusso, G.; Mengoni, A.; Pignatari, M.; et al. Resonance neutron-capture cross-sections of stable magnesium isotopes and their astrophysical implications. *Phys. Rev. C* **2012**, *85*, 044615. [CrossRef]
102. Marganiec, J.; Dillmann, I.; Pardo, C.D.; Käppeler, F.; Walter, S. Stellar (n,γ) cross-sections of p-process isotopes. II. Yb168, W180, Os184, Pt190, and Hg196. *Phys. Rev. C* **2010**, *82*, 035806. [CrossRef]
103. Massimi, C.; Altstadt, S.; Andrzejewski, J.; Audouin, L.; Barbagallo, M.; Bécares, V.; Bečvář, F.; Belloni, F.; Berthoumieux, E.; Billowes, J.; et al. Neutron spectroscopy of ^{26}Mg states: Constraining the stellar neutron source ^{22}Ne(α,n)^{25}Mg. *Phys. Lett. B* **2017**, *768*, 1–6. [CrossRef]
104. Marganiec, J.; Dillmann, I.; Pardo, C.D.; Käppeler, F. Neutron capture cross-sections of W184 and W186. *Phys. Rev. C* **2009**, *80*, 025804. [CrossRef]
105. Koehler, P.E.; Winters, R.R.; Guber, K.H.; Rauscher, T.; Harvey, J.A.; Raman, S.; Spencer, R.R.; Blackmon, J.C.; Larson, D.C.; Bardayan, D.W.; et al. High-resolution neutron capture and transmission measurements, and the stellar neutron-capture cross-section of ^{88}Sr. *Phys. Rev. C* **2000**, *62*, 055803. [CrossRef]
106. Pavetich, S.; Wallner, A.; Martschini, M.; Akhmadaliev, S.; Dillmann, I.; Fifield, K.; Halfon, S.; Heftrich, T.; Käppeler, F.; Lederer-Woods, C.; et al. Accelerator mass spectrometry measurement of the reaction ^{35}Cl(n ,γ)^{36}Cl at keV energies. *Phys. Rev. C* **2019**, *99*, 015801. [CrossRef]
107. Tagliente, G.; Fujii, K.; Milazzo, P.M.; Moreau, C.; Aerts, G.; Abbondanno, U.; Alvarez, H.; Alvarez-Velarde, F.; Andriamonje, S.; Andrzejewski, J.; et al. Neutron capture cross-section of Zr90: Bottleneck in the s-process reaction flow. *Phys. Rev. C* **2008**, *77*, 035802. [CrossRef]
108. Beer, H.; Sedyshev, P.V.; Rochow, W.; Rauscher, T.; Mohr, P. Neutron capture of ^{30}Si. *Nucl. Phys. A* **2002**, *709*, 453–466. [CrossRef]
109. Tagliente, G.; Milazzo, P.M.; Fujii, K.; Aerts, G.; Abbondanno, U.; Álvarez, H.; Alvarez-Velarde, F.; Andriamonje, S.; Andrzejewski, J.; Assimakopoulos, P.; et al. Experimental study of the Zr91(n,γ) reaction up to 26 keV. *Phys. Rev. C* **2008**, *78*, 045804. [CrossRef]
110. Mosconi, M.; Fujii, K.; Mengoni, A.; Domingo-Pardo, C.; Käppeler, F.; Abbondanno, U.; Aerts, G.; Alvarez-Pol, H.; Alvarez-Velarde, F.; Andriamonje, S.; et al. Neutron physics of the Re/Os clock. I. Measurement of the (n,γ) cross-sections of Os186,187,188 at the CERN n_TOF facility. *Phys. Rev. C* **2010**, *82*, 015802. [CrossRef]
111. Heil, M.; Plag, R.; Uberseder, E.; Bisterzo, S.; Käppeler, F.; Mengoni, A.; Pignatari, M. Stellar neutron capture cross-sections of ^{41}K and ^{45}Sc. *Phys. Rev. C* **2016**, *93*, 055807. [CrossRef]
112. Tagliente, G.; Milazzo, P.M.; Fujii, K.; Abbondanno, U.; Aerts, G.; Alvarez, H.; Alvarez-Velarde, F.; Andriamonje, S.; Andrzejewski, J.; Audouin, L.; et al. The Zr92(n,γ) reaction and its implications for stellar nucleosynthesis. *Phys. Rev. C* **2010**, *81*, 055801. [CrossRef]
113. Dillmann, I.; Domingo-Pardo, C.; Heil, M.; Käppeler, F.; Wallner, A.; Forstner, O.; Golser, R.; Kutschera, W.; Priller, A.; Steier, P.; et al. Determination of the stellar (n,γ) cross-section of Ca40 with accelerator mass spectrometry. *Phys. Rev. C* **2009**, *79*, 065805. [CrossRef]
114. Tagliente, G.; Milazzo, P.M.; Fujii, K.; Abbondanno, U.; Aerts, G.; Álvarez, H.; Alvarez-Velarde, F.; Andriamonje, S.; Andrzejewski, J.; Audouin, L.; et al. The ^{93}Zr(n,γ) reaction up to 8 keV neutron energy. *Phys. Rev. C* **2013**, *87*, 014622. [CrossRef]
115. Tagliente, G.; Milazzo, P.M.; Fujii, K.; Abbondanno, U.; Aerts, G.; Alvarez, H.; Alvarez-Velarde, F.; Andriamonje, S.; Andrzejewski, J.; Audouin, L.; et al. Neutron capture on Zr94: Resonance parameters and Maxwellian-averaged cross-sections. *Phys. Rev. C* **2011**, *84*, 015801. [CrossRef]
116. Marganiec, J.; Dillmann, I.; Domingo-Pardo, C.; Käppeler, F. Stellar (n ,γ) cross-sections of neutron-rich nuclei: Completing the isotope chains of Yb, Os, Pt, and Hg. *Phys. Rev. C* **2014**, *90*, 065801. [CrossRef]

117. Wallner, A.; Buczak, K.; Belgya, T.; Bichler, M.; Coquard, L.; Dillmann, I.; Golser, R.; Käppeler, F.; Karakas, A.; Kutschera, W.; et al. Precise measurement of the thermal and stellar ^{54}Fe(n,γ)^{55}Fe cross-sections via accelerator mass spectrometry. *Phys. Rev. C* **2017**, *96*, 025808. [CrossRef]
118. Tagliente, G.; Milazzo, P.M.; Fujii, K.; Abbondanno, U.; Aerts, G.; Álvarez, H.; Alvarez-Velarde, F.; Andriamonje, S.; Andrzejewski, J.; Audouin, L.; et al. ^{96}Zr(n,γ) measurement at the n_TOF facility at CERN. *Phys. Rev. C* **2011**, *84*, 055802. [CrossRef]
119. Heil, M.; Käppeler, F.; Uberseder, E.; Gallino, R.; Pignatari, M. Neutron capture cross-sections for the weak s process in massive stars. *Phys. Rev. C* **2008**, *77*, 015808. [CrossRef]
120. Rapp, W.; Heil, M.; Hentschel, D.; Käppeler, F.; Reifarth, R.; Brede, H.J.; Klein, H.; Rauscher, T. α- and neutron-induced reactions on ruthenium isotopes. *Phys. Rev. C* **2002**, *66*, 015803. [CrossRef]
121. Koehler, P.E.; Guber, K.H. Improved ^{192,194,195,196}Pt(n,γ) and ^{192}Ir(n,γ) astrophysical reaction rates. *Phys. Rev. C* **2013**, *88*, 035802. [CrossRef]
122. Žugec, P.; Barbagallo, M.; Colonna, N.; Bosnar, D.; Altstadt, S.; Andrzejewski, J.; Audouin, L.; Becares, V.; Bečvář, F.; Belloni, F.; et al. Experimental neutron capture data of ^{58}Ni from the CERN n_TOF facility. *Phys. Rev. C* **2014**, *89*, 014605. [CrossRef]
123. Guber, K.H.; Derrien, H.; Leal, L.C.; Arbanas, G.; Wiarda, D.; Koehler, P.E.; Harvey, J.A. Astrophysical reaction rates for Ni58,60(n,γ) from new neutron capture cross-section measurements. *Phys. Rev. C* **2010**, *82*, 057601. [CrossRef]
124. Dillmann, I.; Domingo-Pardo, C.; Heil, M.; Käppeler, F.; Walter, S.; Dababneh, S.; Rauscher, T.; Thielemann, F.K. Stellar (n,γ) cross-sections of p-process isotopes Part I: Pd102, Te120, Ba130,132, and Dy156. *Phys. Rev. C* **2010**, *81*, 015801. [CrossRef]
125. Lederer, C.; Massimi, C.; Berthoumieux, E.; Colonna, N.; Dressler, R.; Guerrero, C.; Gunsing, F.; Käppeler, F.; Kivel, N.; Pignatari, M.; et al. Erratum: ^{62}Ni(n,γ) and ^{63}Ni(n,γ) cross-sections measured at the n_TOF facility at CERN [Phys. Rev. C 89, 025810 (2014)]. *Phys. Rev. C* **2015**, *92*, 019903. [CrossRef]
126. Lederer, C.; Massimi, C.; Altstadt, S.; Andrzejewski, J.; Audouin, L.; Barbagallo, M.; Bécares, V.; Bečvář, F.; Belloni, F.; Berthoumieux, E.; et al. Neutron Capture cross-section of Unstable Ni63: Implications for Stellar Nucleosynthesis. *Phys. Rev. L* **2013**, *110*, 022501. [CrossRef] [PubMed]
127. Massimi, C.; Becker, B.; Dupont, E.; Kopecky, S.; Lampoudis, C.; Massarczyk, R.; Moxon, M.; Pronyaev, V.; Schillebeeckx, P.; Sirakov, I.; et al. Neutron capture cross-section measurements for ^{197}Au from 3.5 to 84 keV at GELINA. *Eur. Phys. J. A* **2014**, *50*, 124. [CrossRef]
128. Weigand, M.; Beinrucker, C.; Couture, A.; Fiebiger, S.; Fonseca, M.; Göbel, K.; Heftrich, M.; Heftrich, T.; Jandel, M.; Käppeler, F.; et al. ^{63}Cu(n,γ) cross-section measured via 25 keV activation and time of flight. *Phys. Rev. C* **2017**, *95*, 015808. [CrossRef]
129. Calviño, F.; Cortes, G.; Poch, A.; Pretel, M. The La139(n,γ) cross-section: Key for the onset of the s-process. *Phys. Rev. C* **2007**, *75*, 035807. [CrossRef]
130. Prokop, C.J.; Couture, A.; Jones, S.; Mosby, S.; Rusev, G.; Ullmann, J.; Krtička, M. Measurement of the ^{65}Cu(n,γ) cross section using the Detector for Advanced Neutron Capture Experiments at LANL. *Phys. Rev. C* **2019**, *99*, 055809. [CrossRef]
131. Capote, R.; Lozano Leyva, M.L.; Molina-Coballes, A.; Quesada Molina, J.M.; Marrone, S.; Abbondanno, U.; Aerts, G.; Álvarez Velarde, F. Measurement of the Sm151(n,γ) cross-section from 0.6 eV to 1 MeV via the neutron time-of-flight technique at the CERN n_TOF facility. *Phys. Rev. C* **2006**, *73*, 034604. [CrossRef]
132. Reifarth, R.; Dababneh, S.; Heil, M.; Käppeler, F.; Plag, R.; Sonnabend, K.; Uberseder, E. Neutron activation of natural zinc samples at kT = 25 keV. *Phys. Rev. C* **2012**, *85*, 035802. [CrossRef]
133. Mazzone, A.; Cristallo, S.; Aberle, O.; other 128 authors including Vescovi, D. Measurement of the ^{154}Gd(n,γ) cross-section and its astrophysical implications. *Phys. Lett. B* **2020**, *804*, 135405. [CrossRef]
134. Domingo-Pardo, C.; Abbondanno, U.; Aerts, G.; Álvarez-Pol, H.; Alvarez-Velarde, F.; Andriamonje, S.; Andrzejewski, J.; Assimakopoulos, P.; Audouin, L.; Badurek, G.; et al. Measurement of the neutron capture cross-section of the s-only isotope Pb204 from 1 eV to 440 keV. *Phys. Rev. C* **2007**, *75*, 015806. [CrossRef]
135. Lederer-Woods, C.; Battino, U.; Ferreira, P.; Gawlik, A.; Guerrero, C.; Gunsing, F.; Heinitz, S.; Lerendegui-Marco, J.; Mengoni, A.; Reifarth, R.; et al. Measurement of ^{73}Ge(n,γ) cross-sections and implications for stellar nucleosynthesis. *Phys. Lett. B* **2019**, *790*, 458–465. [CrossRef]
136. Domingo-Pardo, C.; Abbondanno, U.; Aerts, G.; Álvarez, H.; Alvarez-Velarde, F.; Andriamonje, S.; Andrzejewski, J.; Assimakopoulos, P.; Audouin, L.; Badurek, G.; et al. Measurement of the radiative neutron capture cross-section of Pb206 and its astrophysical implications. *Phys. Rev. C* **2007**, *76*, 045805. [CrossRef]
137. Domingo-Pardo, C.; Abbondanno, U.; Aerts, G.; Álvarez-Pol, H.; Alvarez-Velarde, F.; Andriamonje, S.; Andrzejewski, J.; Assimakopoulos, P.; Audouin, L.; Badurek, G.; et al. Resonance capture cross-section of Pb207. *Phys. Rev. C* **2006**, *74*, 055802. [CrossRef]
138. Domingo-Pardo, C.; Abbondanno, U.; Aerts, G.; Álvarez-Pol, H.; Alvarez-Velarde, F.; Andriamonje, S.; Andrzejewski, J.; Assimakopoulos, P.; Audouin, L.; Badurek, G.; et al. New measurement of neutron capture resonances in Bi209. *Phys. Rev. C* **2006**, *74*, 025807. [CrossRef]
139. Vescovi, D.; Mascaretti, C.; Vissani, F.; Piersanti, L.; Straniero, O. The luminosity constraint in the era of precision solar physics. *J. Phys. Nucl. Phys.* **2021**, *48*, 015201. [CrossRef]
140. Chieffi, A.; Domínguez, I.; Limongi, M.; Straniero, O. Evolution and Nucleosynthesis of Zero-Metal Intermediate-Mass Stars. *Astrophys. J.* **2001**, *554*, 1159–1174. [CrossRef]

141. Guandalini, R.; Cristallo, S. Luminosities of carbon-rich asymptotic giant branch stars in the Milky Way. *Astron. Astrophys.* **2013**, *555*, A120. [CrossRef]
142. Cristallo, S.; Abia, C.; Straniero, O.; Piersanti, L. On the Need for the Light Elements Primary Process (LEPP). *Astrophys. J.* **2015**, *801*, 53. [CrossRef]
143. Prantzos, N.; Abia, C.; Cristallo, S.; Limongi, M.; Chieffi, A. Chemical evolution with rotating massive star yields II. A new assessment of the solar s- and r-process components. *Month. Not. R. Astron. Soc.* **2020**, *491*, 1832–1850. [CrossRef]
144. Vescovi, D.; Cristallo, S.; Busso, M.; Liu, N. Magnetic-buoyancy-induced Mixing in AGB Stars: Presolar SiC Grains. *Astrophys. J. Lett.* **2020**, *897*, L25. [CrossRef]
145. Nordhaus, J.; Busso, M.; Wasserburg, G.J.; Blackman, E.G.; Palmerini, S. Magnetic Mixing in Red Giant and Asymptotic Giant Branch Stars. *Astrophys. J. Lett.* **2008**, *684*, L29. [CrossRef]
146. Denissenkov, P.A.; Pinsonneault, M.; MacGregor, K.B. Magneto-Thermohaline Mixing in Red Giants. *Astrophys. J.* **2009**, *696*, 1823–1833. [CrossRef]
147. Busso, M.; Vescovi, D.; Palmerini, S.; Cristallo, S.; Antonuccio-Delogu, V. s-processing in AGB Stars Revisited. III. Neutron Captures from MHD Mixing at Different Metallicities and Observational Constraints. *Astrophys. J.* **2021**, *908*, 55. [CrossRef]
148. Acheson, D.J.; Gibbons, M.P. On the Instability of Toroidal Magnetic Fields and Differential Rotation in Stars. *Philos. Trans. R. Soc. Lond. Ser. A* **1978**, *289*, 459–500. [CrossRef]
149. Magrini, L.; Vescovi, D.; Casali, G.; Cristallo, S.; Viscasillas Vázquez, C.; Cescutti, G.; Spina, L.; Van Der Swaelmen, M.; Randich, S. Magnetic-buoyancy-induced mixing in AGB stars: a theoretical explanation of the non-universal relation of [Y/Mg] to age. *Astron. Astrophys.* **2021**, *646*, L2. [CrossRef]
150. Zinner, E. 1.4—Presolar Grains. In *Treatise on Geochemistry*, 2nd ed.; Holland, H.D., Turekian, K.K., Eds.; Elsevier: Oxford, UK, 2014; pp. 181–213. [CrossRef]
151. Liu, N.; Savina, M.R.; Gallino, R.; Davis, A.M.; Bisterzo, S.; Gyngard, F.; Käppeler, F.; Cristallo, S.; Dauphas, N.; Pellin, M.J.; et al. Correlated Strontium and Barium Isotopic Compositions of Acid-cleaned Single Mainstream Silicon Carbides from Murchison. *Astrophys. J.* **2015**, *803*, 12. [CrossRef]
152. Hoppe, P.; Annen, P.; Strebel, R.; Eberhardt, P.; Gallino, R.; Lugaro, M.; Amari, S.; Lewis, R.S. Meteoritic Silicon Carbide Grains with Unusual Si Isotopic Compositions: Evidence for an Origin in Low-Mass, Low-Metallicity Asymptotic Giant Branch Stars. *Astrophys. J. Lett.* **1997**, *487*, L101–L104. [CrossRef]
153. Lewis, K.M.; Lugaro, M.; Gibson, B.K.; Pilkington, K. Decoding the Message from Meteoritic Stardust Silicon Carbide Grains. *Astrophys. J. Lett.* **2013**, *768*, L19. [CrossRef]
154. Gail, H.P.; Zhukovska, S.V.; Hoppe, P.; Trieloff, M. Stardust from Asymptotic Giant Branch Stars. *Astrophys. J.* **2009**, *698*, 1136–1154. [CrossRef]
155. Cristallo, S.; Nanni, A.; Cescutti, G.; Minchev, I.; Liu, N.; Vescovi, D.; Gobrecht, D.; Piersanti, L. Mass and metallicity distribution of parent AGB stars of presolar SiC. *Astron. Astrophys.* **2020**, *644*, A8. [CrossRef]
156. Lugaro, M.; Cseh, B.; Világos, B.; Karakas, A.I.; Ventura, P.; Dell'Agli, F.; Trappitsch, R.; Hampel, M.; D'Orazi, V.; Pereira, C.B.; et al. Origin of Large Meteoritic SiC Stardust Grains in Metal-rich AGB Stars. *Astrophys. J.* **2020**, *898*, 96. [CrossRef]
157. Nicolussi, G.K.; Davis, A.M.; Pellin, M.J.; Lewis, R.S.; Clayton, R.N.; Amari, S. s-Process Zirconium in Presolar Silicon Carbide Grains. *Science* **1997**, *277*, 1281–1284. [CrossRef]
158. Barzyk, J.G.; Savina, M.R.; Davis, A.M.; Gallino, R.; Gyngard, F.; Amari, S.; Zinner, E.; Pellin, M.J.; Lewis, R.S.; Clayton, R.N. Constraining the 13C neutron source in AGB stars through isotopic analysis of trace elements in presolar SiC. *Meteorit. Planet. Sci.* **2007**, *42*, 1103–1119. [CrossRef]
159. Liu, N.; Savina, M.R.; Davis, A.M.; Gallino, R.; Straniero, O.; Gyngard, F.; Pellin, M.J.; Willingham, D.G.; Dauphas, N.; Pignatari, M.; et al. Barium Isotopic Composition of Mainstream Silicon Carbides from Murchison: Constraints for s-process Nucleosynthesis in Asymptotic Giant Branch Stars. *Astrophys. J.* **2014**, *786*, 66. [CrossRef]
160. Liu, N.; Stephan, T.; Boehnke, P.; Nittler, L.R.; O'D. Alexander, C.M.; Wang, J.; Davis, A.M.; Trappitsch, R.; Pellin, M.J. J-type Carbon Stars: A Dominant Source of ^{14}N-rich Presolar SiC Grains of Type AB. *Astrophys. J. Lett.* **2017**, *844*, L12. [CrossRef]
161. Trappitsch, R.; Stephan, T.; Savina, M.R.; Davis, A.M.; Pellin, M.J.; Rost, D.; Gyngard, F.; Gallino, R.; Bisterzo, S.; Cristallo, S.; et al. Simultaneous iron and nickel isotopic analyses of presolar silicon carbide grains. *Geochim. Cosmochim. Acta* **2018**, *221*, 87–108.
162. Stephan, T.; Trappitsch, R.; Davis, A.M.; Pellin, M.J.; Rost, D.; Savina, M.R.; Jadhav, M.; Kelly, C.H.; Gyngard, F.; Hoppe, P.; et al. Strontium and barium isotopes in presolar silicon carbide grains measured with CHILI—Two types of X grains. *Geochim. Cosmochim. Acta* **2018**, *221*, 109–126.
163. Stephan, T.; Trappitsch, R.; Hoppe, P.; Davis, A.M.; Pellin, M.J.; Pardo, O.S. Molybdenum Isotopes in Presolar Silicon Carbide Grains: Details of s-process Nucleosynthesis in Parent Stars and Implications for r- and p-processes. *Astrophys. J.* **2019**, *877*, 101. [CrossRef]
164. Palmerini, S.; Trippella, O.; Busso, M.; Vescovi, D.; Petrelli, M.; Zucchini, A.; Frondini, F. *s*-Processing from MHD-induced mixing and isotopic abundances in presolar SiC grains. *Geochim. Cosmochim. Acta* **2018**, *221*, 21–36. [CrossRef]
165. Palmerini, S.; Busso, M.; Vescovi, D.; Naselli, E.; Pidatella, A.; Mucciola, R.; Cristallo, S.; Mascali, D.; Mengoni, A.; Simonucci, S.; et al. Presolar Grain Isotopic Ratios as Constraints to Nuclear and Stellar Parameters of Asymptotic Giant Branch Star Nucleosynthesis. *Astrophys. J.* **2021**, *921*, 7. [CrossRef]
166. Grisoni, V.; Romano, D.; Spitoni, E.; Matteucci, F.; Ryde, N.; Jönsson, H. Fluorine in the solar neighbourhood: modelling the Galactic thick and thin discs. *Month. Not. R. Astron. Soc.* **2020**, *498*, 1252–1258. [CrossRef]

167. Jorissen, A.; Smith, V.V.; Lambert, D.L. Fluorine in red giant stars : evidence for nucleosynthesis. *Astron. Astrophys.* **1992**, *261*, 164–187.
168. Abia, C.; Recio-Blanco, A.; de Laverny, P.; Cristallo, S.; Domínguez, I.; Straniero, O. Fluorine in Asymptotic Giant Branch Carbon Stars Revisited. *Astrophys. J.* **2009**, *694*, 971–977. [CrossRef]
169. Abia, C.; Cunha, K.; Cristallo, S.; de Laverny, P.; Domínguez, I.; Eriksson, K.; Gialanella, L.; Hinkle, K.; Imbriani, G.; Recio-Blanco, A.; et al. Fluorine Abundances in Galactic Asymptotic Giant Branch Stars. *Astrophys. J. Lett.* **2010**, *715*, L94–L98. [CrossRef]
170. Abia, C.; Cunha, K.; Cristallo, S.; de Laverny, P.; Domínguez, I.; Recio-Blanco, A.; Smith, V.V.; Straniero, O. The First Fluorine Abundance Determinations in Extragalactic Asymptotic Giant Branch Carbon Stars. *Astrophys. J. Lett.* **2011**, *737*, L8. [CrossRef]
171. Abia, C.; Cristallo, S.; Cunha, K.; de Laverny, P.; Smith, V.V. Additional fluorine abundance determinations in evolved stars. *Astron. Astrophys.* **2019**, *625*, A40. [CrossRef]
172. Lucatello, S.; Masseron, T.; Johnson, J.A.; Pignatari, M.; Herwig, F. Fluorine and Sodium in C-rich Low-metallicity Stars. *Astrophys. J.* **2011**, *729*, 40. [CrossRef]
173. Goriely, S.; Mowlavi, N. Neutron-capture nucleosynthesis in AGB stars. *Astron. Astrophys.* **2000**, *362*, 599–614.
174. Lugaro, M.; Ugalde, C.; Karakas, A.I.; Görres, J.; Wiescher, M.; Lattanzio, J.C.; Cannon, R.C. Reaction Rate Uncertainties and the Production of ^{19}F in Asymptotic Giant Branch Stars. *Astrophys. J.* **2004**, *615*, 934–946. [CrossRef]
175. Cristallo, S.; Di Leva, A.; Imbriani, G.; Piersanti, L.; Abia, C.; Gialanella, L.; Straniero, O. Effects of nuclear cross-sections on ^{19}F nucleosynthesis at low metallicities. *Astron. Astrophys.* **2014**, *570*, A46. [CrossRef]
176. Abia, C.; Cunha, K.; Cristallo, S.; de Laverny, P. The origin of fluorine: abundances in AGB carbon stars revisited. *Astron. Astrophys.* **2015**, *581*, A88. [CrossRef]
177. Limongi, M.; Chieffi, A. Presupernova Evolution and Explosive Nucleosynthesis of Rotating Massive Stars in the Metallicity Range -3 $\leq$ [Fe/H] $\leq$ 0. *Astrophys. J. Suppl.* **2018**, *237*, 13. [CrossRef]
178. Casali, G.; Spina, L.; Magrini, L.; Karakas, A.I.; Kobayashi, C.; Casey, A.R.; Feltzing, S.; Van der Swaelmen, M.; Tsantaki, M.; Jofré, P.; et al. The Gaia-ESO survey: The non-universality of the age-chemical-clocks-metallicity relations in the Galactic disc. *Astron. Astrophys.* **2020**, *639*, A127. [CrossRef]
179. Liu, N.; Gallino, R.; Cristallo, S.; Bisterzo, S.; Davis, A.M.; Trappitsch, R.; Nittler, L.R. New Constraints on the Major Neutron Source in Low-mass AGB Stars. *Astrophys. J.* **2018**, *865*, 112. [CrossRef]
180. Cristallo, S.; La Cognata, M.; Massimi, C.; Best, A.; Palmerini, S.; Straniero, O.; Trippella, O.; Busso, M.; Ciani, G.F.; Mingrone, F.; et al. The Importance of the ^{13}C(α,n)^{16}O Reaction in Asymptotic Giant Branch Stars. *Astrophys. J.* **2018**, *859*, 105. [CrossRef]